Archimer
https://archimer.ifremer.fr

Late Cretaceous changes in oceanic currents and sediment sources in the eastern Tethys: insights from Nd isotopes and clay mineralogy

Chenot Elise [1, 2, *], Pucéat Emmanuelle [2], Freslon Nicolas [2], Deconinck Jean-François [2], Razmjooei Mohammad Javad [3, 4], Thibault Nicolas [4]

[1] Institut Polytechnique Lasalle Beauvais, 19 Rue Pierre Waguet, BP 30313, F-60026 Beauvais, France
[2] Biogéosciences, UMR 6282, 6 boulevard Gabriel, Université Bourgogne Franche-Comté, F-21000 Dijon, France
[3] Department of Geology, Faculty of Earth Science, Shahid Beheshti University, Tehran, Iran
[4] IGN, Univ. of Copenhagen, Øster Voldgade 10, DK-1350 Copenhagen, Denmark

* Corresponding author : Elise Chenot, email address : chenot@unilasalle.fr

emmanuelle.puceat@u-bourgogne.fr ; nicolas.freslon@u-bourgogne.fr ; jean-francois.deconinck@u-bourgogne.fr ; nt@ign.ku.dk

Abstract :

The Late Cretaceous is marked by geodynamical changes including Africa-Eurasia convergence that resulted in the narrowing of the Tethys Ocean and in ophiolite obduction along the southern margin of the various continental blocks in eastern Tethys. Geochemical and mineralogical analyses were performed on the Shahneshin section (Zagros Basin - eastern Tethys), to explore the consequences of this evolution on oceanic circulation, and to estimate the role of ophiolite weathering that can impact climate through atmospheric CO2 drawdown. [Ni] and [Cr] sharply increase in the uppermost Campanian – Maastrichtian interval and are not coeval with an increase in the Nd isotope composition (εNd) of the detrital fraction of the sediments. This is interpreted as reflecting weathering of the mantellic, ultramafic part of the ophiolite sequence at that time, implying that ophiolites were exposed on the continents as soon as the Coniacian in the vicinity of the Zagros Basin. Hence their weathering could have contributed to the Late Cretaceous climatic cooling. Clay mineralogy reveals an alternation of kaolinite-rich humid periods (Coniacian/Santonian and late early Campanian to latest Campanian) and kaolinite-depleted arid periods (early Campanian and the latest Campanian to late Maastrichtian). The εNd(t) of bathyal waters (carbonate leached fraction) appears quite radiogenic, in the range of -3.4 to -5.2 ε-units, about 2 to 4 ε-units higher than the detrital fraction. Changes in the εNd(t) of detrital material delivered to the Zagros Basin appear to control the εNd(t) of the local bottom waters from the Coniacian to the middle Campanian. By contrast, decoupling of detrital εNd(t) from that of the local bottom waters from the middle Campanian to the Maastrichtian points to increasing fluxes of westward flowing Pacific radiogenic water masses into the eastern Tethys at that time. These results support an intensification of the Tethyan Circumglobal Current, likely related to the narrowing of the Tethyan seaway.

Highlights

► Alternating humid and arid periods throughout the Late Cretaceous of Zagros. ► Ophiolite sequence was aerially exposed as soon as the Coniacian in the Zagros area. ► Intensification of the TCC from the middle Campanian to the Maastrichtian.

1. Introduction

The Late Cretaceous was characterized by a long-term global cooling (Huber et al., 1995, 2002, 2018; Pucéat et al., 2003; Friedrich et al. 2012; Linnert et al., 2014) which has been linked to a decrease in atmospheric pCO_2 (Royer et al., 2012; Franks et al., 2014; Wang et al., 2014; Mills et al., 2019). During the last decades, many studies have investigated the processes involved in this atmospheric CO_2 evolution. A reduction in CO_2 mantle degassing, linked to a reduction in seafloor production rates and continental arc magmatism, has been repeatedly invoked to explain a decrease in pCO_2 during the Late Cretaceous (Cogné and Humler, 2006; Van der Meer et al., 2014; McKenzie et al., 2016). Enhanced CO_2 drawdown

by continental weathering has also been suggested as a driver of this climate evolution (Jagoutz et al., 2016; Chenot et al., 2018), with a potentially important role of ophiolite obduction and weathering onto the southern Tethyan margin recently pointed out by Jagoutz et al. (2016). Whilst some constraints have been brought on the timing of the initiation of ophiolite obduction, notably using radiometric geochemical dating (Delaloye and Desmons, 1980; Lanphere and Pamić, 1983; Shahidi and Nazari, 1997; Tilton et al., 1981; Babaie et al., 2006; Shafaii Moghadam and Stern, 2011; Agard et al., 2011; Ao et al., 2016), information is still largely lacking on the timing of effective subaerial exposure of ophiolitic rocks to weathering processes, that can only be inferred from biostratigraphy of the overlying sediments (Shafaii Moghadam and Stern, 2015). This lack of information impedes our knowledge of the links between climate and obduction during the Late Cretaceous.

The ophiolite obduction that affected a large part of the southern Tethyan margin has been related to the dynamics of Africa-Eurasia convergence (Guiraud and Bosworth, 1997; Şengör and Stock, 2014; Jolivet et al., 2016). This convergence also resulted in a narrowing of the Tethys Ocean, with potential implications on oceanic circulation, a major component of the climate system. A major reorganization in the global oceanic circulation has been depicted during the Late Cretaceous, evidenced during the Campanian by a decrease of 2 ε-units of the Nd isotope composition of bottom waters, a tracer of modern and ancient ocean circulation, in the Atlantic and Indian oceans (Robinson et al., 2010; Macleod et al., 2011; Murphy and Thomas, 2012, 2013; Robinson and Vance, 2012; Voigt et al., 2013; Moiroud et al., 2016). This 2 ε-units decrease could have marked the onset or intensification of deep-water formation in the southern Atlantic (Robinson et al., 2010; Robinson and Vance, 2012; Murphy and Thomas, 2012, 2013; Voigt et al., 2013) or in the northern Atlantic (Macleod et al., 2011). The progressive narrowing of the Tethys during the Late Cretaceous, related to the northward motion of Africa, may have played a role in this reorganization of the oceanic

circulation. The Tethys Ocean linked the proto-Indian and Atlantic oceans during the Cretaceous, and formed, along with the open Caribbean seaway linking the Atlantic and Pacific Oceans, a low-latitude seaway where seawater could flow unimpeded throughout the globe. A large circum global current, called the Tethyan Circumglobal Current (TCC), is thought to have flowed westward throughout this seaway (Föllmi et al., 1992; Pucéat et al., 2005; Soudry et al., 2006). Like the modern Antarctic Circum global Current that flows unimpeded around Antarctica, the TCC could have played a major role in the global oceanic circulation, impacting the density balance between oceanic water masses through the transport of salty waters. The development of intensive upwelling systems along the southern Tethyan margin during the Campanian and Maastrichtian, which is marked by large phosphorite deposits and high productivity of floro-faunal assemblages (*e.g.* Notholt, 1985; Almogi-Labin et al., 1993; Eshet and Almogi-Labin, 1996; Ashkenazi-Polivoda et al., 2011), points to potentially important modifications in the intensity of the TCC at that time.

In this context, we aim in this study at exploring the potential changes in the TCC during the narrowing of the Tethys Ocean in the Late Cretaceous. We present a new dataset of the $\varepsilon_{Nd(t)}$ of seawater inferred from the acetic acid-leached fraction of sediments collected along the Shahneshin section (Zagros Basin, Iran), following recent development for the acquisition of a seawater signal from different sediment fractions (Wilson et al., 2013). The Shahneshin outcrop is located in the eastern part of the Tethys, close to the eastern entrance into the Tethyan seaway. The $\varepsilon_{Nd(t)}$ of seawater at this site has thus the potential to track changes in the TCC intensity. The evolution of clay mineral assemblages, of the $\varepsilon_{Nd(t)}$ of the insoluble residual fraction of the sediment, and elemental (Ni and Cr) concentrations of the sediments are also determined, to discuss the possible impact of changes in the source of material eroded from the nearby continent on local seawater $\varepsilon_{Nd(t)}$ and to discuss the potential links between weathering and erosion processes in this region, ophiolite obduction, and

climate.

2. Geodynamical framework and palaeogeography

The Middle East region presents highly deformed sedimentary structures in the orogenic areas (Zagros, Caucasus) and metamorphic rocks around the obducted areas (Cyprus, Northern Turkey, Syria, south of Iran, Oman; Fig. 1). This modern geological framework is linked to the anticlockwise movement of Africa initiated during the Cretaceous, which ultimately led to the closure of the Tethyan Realm and to the subduction of the Neo-Tethys Ocean beneath central Iran (Bosworth et al., 1999; Jolivet et al., 2016). In the eastern part of the Tethys, this tectonic event is expressed by a 5 000 km-long region of relief developed across the north of Africa and the Middle East called the Ayyubid orogeny. It is associated to the establishment of a widespread ophiolite belt along the Afro-Arabian passive continental margin during the Turonian to Campanian interval (Agard et al., 2005; Homke et al., 2009; Shafaii Moghadam and Stern, 2011; Şengör and Stock, 2014; Jolivet et al., 2016; Fig. 1). This compressional tectonic regime has induced the development of highly subsiding basins and inversion reliefs (*e.g.* Zagros folded zone; Koop and Stoneley, 1982; Agard et al., 2005; Homke et al., 2009; Şengör and Stock, 2014). Weathering of newly created nearby continental masses most likely provided detrital particles transported and deposited into adjacent highly subsiding basins (Saura et al., 2011).

2.1. Zagros basin and the "Gurpi" Formation

The Zagros folded zone encompasses south-eastern Turkey, northern Syria, northern Iraq and western to southern parts of Iran (Alavi, 1980, 1994; Berberian and King, 1981; Dercourt et al., 1986; Fig. 1a). In the west and southwestern parts of Iran, this NW-SE folded structure is composed of four main mountains provinces called Lurestan, Khuzestan, Internals Fars and Coastal Fars at about 26 to 35° N (Agard et al., 2005; Fig. 1a). Palaeogeographical reconstructions suggest a palaeolatitude of 5 to 10° N for the Zagros Basin during the

Campanian and Maastrichtian (Philip and Floquet, 2000; Barrier and Vrielynck, 2007; Fig. 1b-c). This basin is located within the equatorial Tethyan corridor, bordered to the south by the Arabian Shield, and to the north by an active subduction zone with ophiolitic nappes, possibly above sea-level during the early Campanian and immersed during the late Maastrichtian (Barrier and Vrielynck, 2007; Fig 1b-c). The ages of the sediments overlying the mantellic and crustal rocks, that provide an age range of the sub-aerial exposure of the Iranian Zagros ophiolites, are Triassic to Cretaceous for Kermanshah ophiolites (Lurestan; Saccani et al., 2013; Whitechurch et al., 2013; Shafaii Moghadam and Stern, 2015), Cenomanian-Turonian to early Santonian for Neyriz ophiolites (Babaei et al., 2006; Shafaii Moghadam and Stern, 2011), undifferentiated Late Cretaceous for Haji Abad ophiolites (Ghasemi et al., 2002), and late Turonian to Maastrichtian for Baft ophiolites (Fars Provinces; Shafaii Moghadam and Stern, 2011; Shafaii Moghadam et al., 2013).

The Late Cretaceous sedimentation of the Zagros Basin (Coniacian to Maastrichtian) consists of organic matter-rich marls and limestones which compose the Gurpi Formation (Fm. - average of 3% of total organic carbon; Ala et al., 1980). This formation is largely outcropping in the four main Zagros mountain provinces (Fig. 1c). Several hiatuses are recorded in the Gurpi Fm. which have been related to maximum flooding surfaces and/or tectonic events (Razmjooei et al., 2014, 2018, 2020a; Zarei and Ghasemi-Nejad, 2015). The dinoflagellate diversity associated to the microfossil assemblages (planktonic and benthic foraminifera) highlight the existence of lateral variability of facies in the Gurpi Fm. The Fars province displays external ramp environments whereas the Lurestan and the Khuzestan Province record shallower environments characterized by two bioturbated and fossiliferous limestones units called the "*Lopha* limestone member" (late Campanian, *Globotruncana aegyptica* biozone) and the "Emam Hassan member" (late Campanian to early Maastrichtian, *Gansserina gansseri* biozone; Zarei and Ghasemi-Nejad, 2015). This facies lateral variability

recorded in the Gurpi Fm., associated to regional gaps, has been linked to compressive tectonic movements generating different subsidence rates between provinces.

2.2. Shahneshin section

The investigated Late Cretaceous deposits of the Gurpi Fm. are located in the central part of the Zagros folded zone, west of the Fars province, to the north east of Kazerun city and the north west of the Shahneshin anticline (N 29° 44' 47" and E 51° 46' 31" for the base and 29° 44' 40.69" and E 51° 46' 26.87" for the top of the studied interval at Shahneshin). At Shahneshin, the sediments are composed of dark grey marls and light yellow argillaceous limestones alternations (Fig. 2). The marls and marly limestones of the Gurpi Fm. have been deposited in a deep sedimentary basin (Motiei, 1993). Hemmati-Nasab et al. (2008) and Darabi et al. (2018) respectively suggest rough estimations of 800 to 1200m and 450 to 600m paleo-water depth for the Gurpi Fm. in Lurestan area. Occurrence of a very high abundance of benthic foraminifers in the upper Campanian of Shahneshin suggests a much shallower condition at this time, which could be due to a tectonically-induced regression caused by a phase of uplift (Razmjooei et al., 2018, 2020a).

The age-model relies on the integrated stratigraphic study of the Shahneshin section by Razmjooei et al. (2018; Fig. 3). Slight modifications were however proposed later on by Razmjooei et al. (2020a) for the basal part of the section based on carbon-isotope stratigraphy. In particular, the authors applied in Razmjooei et al. (2018) the biostratigraphic concept of the Coniacian/Santonian boundary based on the first occurrence of nannofossil *L. cayeuxii* at 20m. In Razmjooei et al. (2020a), the authors argued for the level of the Kingsdown carbon isotope event at 40 m being the best possible marker for the Coniacian/Santonian boundary, assuming some degree of plankton diachronism. This interpretation is kept here. Subsequently, the age-model applied here considers eight anchor points (Table 1; Suppl. Fig. 1). Out of these, the base Maastrichtian at 72.15 Ma is at the level identified in Razmjooei et

al. (2018) but also accounts immediately for a ca. 2 Myr hiatus truncating the late Campanian (Suppl. Fig. 1). The FO of *G. aegyptiaca*, LO of *M. furcatus* and LO of *D. asymetrica* are given as in Razmjooei et al. (2018) age-model, the Kingsdown event is considered as the level of the Coniacian/Santonian boundary at 86.49 Ma and the basal 40 m of the section are considered to follow a similar sedimentation rate of 2.36cm/kyr as the interval above between 40 and 94m, thus giving an age of 88.19 Ma for the base of the section. This well-constrained age model reveals important changes in the sedimentation rate along the section, from approximately 2.4cm/kyr in the upper Coniacian to Santonian, around 0.6cm/kyr in the lowermost Campanian, to 2.5cm/kyr in the remaining of the Campanian. A significant gap, possibly of up to 2 Ma, has been suggested to occur also in the uppermost Campanian to lowermost Maastrichtian, at 280 to 290m (Razmjooei et al., 2018; Suppl. Fig. 1).

3. Material and methods

3.1. Clay mineralogy

For detailed fieldwork and sampling strategy, we refer here to Razmjooei et al. (2018). Our sampling resolution for clay mineralogy varies between 1m and 5m. Mineralogical analyses have been performed at the Biogéosciences Laboratory (University of Bourgogne-Franche Comté, Dijon, France). Clay mineral assemblages of 120 samples have been identified by X-ray diffraction (XRD) on oriented mounts of non-calcareous clay-sized particles (<2 μm). The procedure described by Moore and Reynolds (1997) has been used to prepare the samples. Diffractograms have been obtained using a Bruker D4 Endeavor diffractometer with CuK_α radiations with LynxEye detector and Ni filter, under 40-kV voltage and 25-mA intensity. Three preparations have been analysed, after air-drying, after ethylene-glycol solvation and after heating at 490°C for 2h (Fig. 4). The goniometer scanned from 2.5° to 28.5° for each run. Clay minerals have been identified by the position of their main diffraction peaks on the three XRD runs, while semi-quantitative estimates have been

produced in relation to their area (Moore and Reynolds, 1997). Areas have been determined on diffractograms of glycolated runs with MacDiff 4.2.5. Software (Petschick, 2000). Beyond the evaluation of the absolute proportions of the clay minerals, the aim was to identify their relative fluctuations along the section.

3.2. Rare earth elements concentrations (REE) and neodymium (Nd) isotope analyses

3.2.1. Sample preparation: carbonate and insoluble fraction extraction

Eighteen sedimentary bulk rock samples from the Shahneshin section were finely crushed using an agate mortar and pestle. Aliquots of about 1.5g of powdered sediments were leached with 20ml of acetic acid solution (2%) during 30 minutes in Teflon vial (Savillex®). This short leaching time using quite diluted acetic acid aims to dissolve part of the carbonates while limiting extraction of Fe-Mn oxides and/or reactive minerals (Wilson et al., 2013). The solution was filtered (0.45μm, PTFE), evaporated to dryness and then re-dissolved with 4M hydrochloric acid (HCl).

Another aliquot of about 2g of each powdered sediment sample went through the 3-step leaching procedure derived from Bayon et al. (2002). Carbonate was removed using 20ml acetic acid (10%, AA) that reacted overnight (about 18h), then Fe-Mn oxides were removed using a 20ml reductive solution (25% acetic acid + 1M Hydroxylammonium Hydrochloride, AA+HH) during 6 hours, and organic matter was removed using a 5% hydrogen peroxide solution (H_2O_2, %wt/v) that reacted overnight (Tessier et al., 1979; Bayon et al., 2002). About 100mg of the residue was then digested using alkaline fusion following Bayon et al. (2009) and the precipitated Fe-oxy-hydroxides dissolved in 4M hydrochloric acid (HCl).

3.2.2. Determination of the REE concentrations

Trace elements abundances in the carbonate leachates and the residue were determined using an aliquot of the final mother solutions diluted in 10 ml HNO_3 2% (v/v). The REE concentrations were measured with a quadrupole inductively coupled plasma mass

spectrometer (Thermo X-Series II) at the "Pôle Spectrométrie Océan" (IUEM Brest, France), using the Tm addition method (Barrat et al., 1996; Bayon et al., 2009). The REE were measured in low resolution mode, and polyatomic oxide and hydroxide interferences were corrected using oxide formation rates determined by analyzing solutions of ultrapure water, Ba + Ce, Pr + Nd and Sm + Eu + Gd + Tb at the beginning of the measurement cycle. The uncertainty on all measurements was better than 5% for REE. The accuracy of the method was monitored by repeated analyses of two certified reference materials from USGS (BHVO-2 and BCR-2); deviation from the certified values (Jochum et al., 2016) was better than 5% for all replicates.

3.2.3. Determination of the Nd isotopic composition

The REE were isolated using common ion exchange chromatography, including a first ion exchange resin to isolate the lanthanides (AG-50W-X8, Bio-Rad) and a second one (Ln resin, Eichrom) to isolate Nd (Bayon et al., 2012). The Nd isotopic compositions of the residues were carried on a Multi-Collector MC-ICP-MS (Neptune, Thermo Scientific) at the "Pôle Spectrométrie Océan" (IFREMER Brest, France) with instrumental bias corrected by a sample-standard bracketing method, using *JNdi-1* (Tanaka et al., 2000). The carbonate leachate Nd isotope compositions were determined at the LGLTPE laboratory in Lyon (Ecole Normale Supérieure de Lyon, France) on a Thermo Scientific Neptune and a Nu Plasma 1700 MC-ICP-MS, using the *Rennes in-house* Nd standard (Chauvel and Blichert-Toft, 2001) as internal standard. All ^{143}Nd/^{144}Nd ratios were normalized to a value of 0.7219 for ^{146}Nd/^{144}Nd (Table 2). The 2s external reproducibility of our measurements was estimated using repeated analyses of the *JNdi-1* (0.512115 ± 0.000016; average ± 2s) and the *Rennes in-house* Nd standard (0.511961 ± 0.000009). The overall reproducibility of the chemistry is estimated by repeated analyses of the BHVO-2 certified reference material. During the course of the study, the measured ^{143}Nd/^{144}Nd ratios of BHVO-2 were 0.512987 ± 0.000005 (average ± 2s; n=5)

and 0.512988 ± 0.000007 (n=12) by using the *JNdi-1* and the *Rennes in-house* Nd as internal standard, respectively. Those values agree well with the reference values for MC-ICP-MS and TIMS measurements (respectively 0.512990 ± 0.000010 and 0.512984 ± 0.000011; Weis et al., 2006).

3.2.4. Post-sedimentation decay correction

The present-day Nd isotopic ratios measured in the samples were corrected for the radioactive decay of ^{147}Sm to ^{143}Nd using the measured Sm and Nd concentrations determined for each sample (^{147}Sm/^{144}Nd = 0.6049 x [Sm]/[Nd]) and a radioactive decay constant λ = 6.539.10^{-12} yr^{-1} for the Sm-Nd system (Begemann et al., 2001). The absolute ages of the Shahneshin samples were calculated using the age model described in the Part 2.2 above and in Table 1. The age-corrected isotopic ratios are expressed using the standard $\varepsilon_{Nd(t)}$ notation, which corresponds to the relative deviation in part per thousand from the Chondritic Uniform Reservoir (CHUR) values at the deposition age, using the present-day ^{143}Nd/^{144}Nd ratio of 0.512630 and ^{147}Sm/^{144}Nd ratio of 0.1960 for the CHUR (Bouvier et al., 2008). The analytical uncertainties expressed under the $\varepsilon_{Nd(t)}$ notation, estimated by propagating external errors introduced by the ^{143}Nd/^{144}Nd (±0.000016 or ±0.000009, ±2σ) and ^{147}Sm/^{144}Nd (±0.004, ±2σ), are ±0.35 for the insoluble fractions and ±0.21 for the carbonate leachates (Table 2).

3.3. Determination of major and trace element concentrations

Twenty-two bulk sediment samples were additionally analysed for their major (Al) and trace-element (Ni, Cr) concentrations at the Service d'Analyse des Roches et des Minéraux of the Centre National de la Recherche Scientifique (SARM, Vandœuvre-lès-Nancy, France). Complete analytical procedure developed at the SARM is detailed in Carignan et al. (2001). About 300mg of powdered rock samples are fused in Pt crucibles with ultrapure LiBO$_2$ at 980°C in an oven for 60 min, and after cooling the fusion glass is dissolved in a HNO$_3$ (1 mol/l) - H$_2$O$_2$ (0.5% v/v) – glycerol (10% v/v) mixture. The samples

were analysed on an ICP-OES (Thermo Fisher iCap 6500) and an ICP-MS (Thermo Fisher iCapQ), respectively, at the Service d'Analyse des Roches et des Minéraux of the Centre National de la Recherche Scientifique (SARM, Vandœuvre-lès-Nancy, France). Uncertainties in measurements, based on analyses of international reference standards (BR, AN-G, UB-N, DR-N, and GH; Govindaraju, 1995) and replicates are lower than 15% for Al_2O_3, and 5% for Ni and Cr (Table 2).

In order to discriminate changes in nickel (Ni) and chromium (Cr) concentration of the detrital material from variations in detrital supply, trace element concentrations have been normalized to Al, as aluminum is considered as a robust tracer of detrital input, and are expressed as element/Al (X/Al) ratios in this study (Fig. 3).

4. Results

4.1. Clay mineralogical assemblages

Clay mineral assemblages of the Shahneshin section are composed of illite-smectite mixed-layers (I-S R1), illite, kaolinite, chlorite, and likely a mixture of random mixed-layers including chlorite-smectite (C-S), chlorite-vermiculite (C-V) and finally vermiculite whose presence is suggested by the relatively narrow reflection at 14 Å which is not modified after saturation with ethylene-glycol and which decreases sharply after heating (Fig. 4). From the base to 260m, I-S R1 dominates the clay fraction (35 to 40%) and decreases to 20% from 260m to the top of the section. Four mineralogical intervals are identified:

- Interval 1 (Coniacian-Santonian):

From the base to 80m, illite (20 to 30%) is associated to I-S R1 and abundant kaolinite reaching 50% at the base of the section and showing a mixture of C-S and C-V (and vermiculite?; 10%) decreasing proportions upward.

- Interval 2 (lowermost Campanian *pars*):

From 80 to 130m, the interval is characterized by increasing proportions of illite and I-S R1

and by the absence of kaolinite. Chlorite is occasionally abundant (up to 30%).

-    Interval 3 (lower Campanian *pars* to upper Campanian):

From 130m to 250m, illite and I-S R1 decrease up section to 15% and less than 40% respectively. The proportions of chlorite never exceed 10%, while the proportions of kaolinite progressively increase up to 40% from the base to the top of the interval.

-    Interval 4 (uppermost Campanian and Maastrichtian):

From 250m to the top of the section, chlorite and illite increase again (respectively 35% and 20%). In the same interval, the mixture of C-S, C-V and vermiculite increases significantly around 30%.

4.2. REE concentrations and Nd isotopes

REE concentrations for the insoluble fractions and the acetic acid leachates are reported on Table 2 and are presented on Fig. 5 normalized to PAAS (Post Archean Australian Shale; Taylor and McLenan, 1985). The insoluble fractions all display quite similar REE patterns, characterized by depletion in Middle Rare Earth Element (MREE) and a very small or absent cerium (Ce) anomaly. By contrast, the acid acetic leachates of all samples display a negative Ce anomaly and enrichment in middle and heavy REEs, with lower REEs concentrations compared to the insoluble fraction. The acetic acid leachates yield systematically more radiogenic Nd isotopic values than the corresponding insoluble fractions, of about 3 ε-units on average, but up to about 4 ε-units (Table 2; Fig. 3). The insoluble fraction $\varepsilon_{Nd(t)}$ ranges from -9.0 to -6.0 ε-units and shows a positive excursion encompassing an interval from the Coniacian to the uppermost Santonian, with $\varepsilon_{Nd(t)}$ reaching maximum values of about -6 ε-units during the Santonian. Insoluble fraction $\varepsilon_{Nd(t)}$ remains around -8 ε-units, within the exception of one sample (ShG E07) that yield a value of -6.8 ε-units, until the lower Campanian where $\varepsilon_{Nd(t)}$ values increase again by about 2 ε-units, from -8.1 to -6.2 ε-units in the uppermost lower Campanian. $\varepsilon_{Nd(t)}$ values then decrease by about 3 ε-units, down

to -9 ε-units in the upper Maastrichtian at the top of the section. The acetic leachate $\varepsilon_{Nd(t)}$ displays a similar evolution than that of the insoluble fraction, with an offset of about 2-3 ε-units toward more radiogenic values, from the Coniacian to the uppermost Santonian. By contrast, acetic leachate $\varepsilon_{Nd(t)}$ values remain quite stable, around -4 ε-units, until the lower Maastrichtian and then decline slightly from the lower to the upper Maastrichtian down to values of about -4.5 ε-units.

4.3. Major and trace element concentrations

Analytical results for the twenty-two samples are shown in Table 3 and Fig. 3. The chemical data of trace elements show that the CaO, SiO_2 and Al_2O_3 contents ranges are 36-48 wt.%, 7–18 wt.% and 2–7 wt.% respectively, and the chemical data of trace elements show that Ni and Cr contents ranges are 21-83 ppm and 42-101 ppm range. Thus, the bulk rocks of the Shahneshin section are rich in CaO, SiO_2 and Al_2O_3, while depleted in Fe_2O_3, K_2O, TiO_2, and MgO. An important characteristic of these carbonates is the highest proportions of Ni and Cr from 250m to the top of the section (upper Campanian to upper Maastrichtian), showed by markedly higher ratios of Ni/Al and Cr/Al above 250m (Fig. 3).

5. Discussion

5.1. Diagenesis of the clay minerals

To interpret clay mineral assemblages in terms of palaeoenvironments, we have to ensure that post depositional transformations including burial diagenesis did not modify significantly the clay minerals and that their initial sedimentary signal is preserved. In this relatively thick section from a highly tectonised area, thermal influences may be expected to have played a significant role on clay mineral assemblages. The influence of a thermal diagenesis is even more probable that the clay assemblages are devoid of I-S R0 comparable to smectites (Fig. 3). This absence is surprising because in the Tethyan Realm and even all over the globe, the Late Cretaceous is marked by a clay sedimentation largely dominated by

smectites (Chamley, 1989; Chamley et al., 1990; Thiry and Jacquin, 1993; Deconinck and Chamley, 1995; Chenot et al., 2018). Moreover, there is an abundance of I-S R1 and a complex mixture of C-S and C-V mixed-layering which are respectively all intermediate phases of the transformation of smectites into illite and chlorite. However, from the top to the bottom of the section, the proportions of illite, chlorite and mixed-layers do not increase steadily, as would have been expected under a strong influence of burial diagenesis. The preservation of kaolinite, which is also sensitive to burial diagenesis, suggests that maximum burial temperature was not high enough (<150°C, Beaufort et al., 2015) to transform this mineral, whose fluctuations seem to correspond to a primary signal (Fig. 3).

To sum up, it is likely that the initial clay sedimentation included a significant proportion of I-S R0 (smectite) but that these minerals under mild thermal influence turned into I-S R1, C-S and C-V mixed-layers. In addition this is in agreement with the moderate to poor preservation of the nannofossils (Razmjooei et al., 2020b). However, the evolution of the relative proportions of illite, chlorite and kaolinite seem to be mainly a primary signal that can be interpreted in terms of palaeoenvironment and palaeoclimate.

5.2. Climatic control of the clay assemblages of the Shahneshin section

The most striking feature of the clay mineralogy of the Shahneshin section is the alternation of kaolinite-rich intervals with intervals devoid of kaolinite (Fig. 6). The formation of kaolinite in soils requires a high level of hydrolysis and consequently a significant humidity and runoff favoring water renewal. A high temperature accelerates the hydrolysis reactions but humidity is the key parameter to form kaolinite in weathering profiles, (Chamley, 1989; Ruffell et al., 2002). Currently, kaolinite is abundant in weathering profiles that developed mainly at low latitudes. Fluctuations in kaolinite proportion in clay assemblages, especially when they are linked to opposite trends in illite and chlorite that derive from weathering and erosion of the basement in more arid environments, is often

interpreted in terms of changes in humidity/aridity (*eg.* Vanderaveroet et al., 1999; Adatte et al., 2002; Moiroud et al., 2012). Kaolinite can also be reworked from old non-metamorphosed rocks. In this case, it is generally accompanied by primary minerals (illite and chlorite), often abundant in ancient rocks that underwent significant diagenesis (Chenot et al., 2016). On the Shahneshin section, percentages of illite and chlorite do not show the same trends as kaolinite but rather display opposite trends. This suggests that kaolinite is most likely reworked from pedogenic blankets developed at the time of sedimentation, which points to the existence, at the time of kaolinite deposition, of a relatively warm and humid climate. Such climatic conditions are supported by the occurrence of bauxites on emerged peri-Tethyan continental masses during the Late Cretaceous (Bárdossy and Dercourt, 1990), and by the compilation of lithological and paleontological indicators, including vegetation (Otto-Bliesner and Upchurch, 1997; Upchurch et al., 2015). By contrast, the intervals with little or no kaolinite, that present higher proportions of illite and chlorite in the clay mineral assemblages, would then point to a drier climate during these intervals. Interestingly, the locally drier climatic conditions recorded during the late Campanian to Maastrichtian at Shahneshin (mineralogical interval 4, Fig. 3) do not reflect the overall humid conditions (kaolinite up to 60-80%) recorded at other tethyan sites with paleolatitudes comprised between approximately 0 and 25°N (Tunisia, Li et al., 2000; Adatte et al., 2002; Egypt, Tantawy et al., 2001; Keller et al., 2002; Iran, Rostami et al., 2018; Italy; Chenot et al., 2018). This feature may be related to the specific paleogeography of the Zagros region, inducing different local climatic conditions in the Zagros studied area in this interval.

It is thus likely that an evolution in local climate could have contributed to the observed changes in clay mineral assemblages (Fig. 6). More humid conditions in intervals 1 (Coniacian to latest Santonian) and 3 (middle Campanian to earliest late Campanian) could have favoured kaolinite formation, while more arid environments in intervals 2 (early

Campanian) and 4 (late Campanian to late Maastrichtian) rather favoured formation of illite and chlorite. Surface marine temperatures inferred from TEX86 values at a comparable latitude in Israel highlight a cooling of a few degrees from the Coniacian to the early Campanian, but remain relatively stable up to the end of early Maastrichtian and do not show any correspondence with the evolution of clay mineralogy on the remaining of the section (Fig. 6; Alsenz et al., 2013). Yet surface temperatures recorded in Israel (Adheret 1 borehole and PAMA Quarry) are likely affected by the development of a large upwelling system during the Campanian and Maastrichtian, depicted by the occurrence of large phosphorite deposits and floro-faunal assemblages of high productivity (Notholt, 1985; Almogi-Labin et al., 1993; Ashckenazi-Polivoda et al., 2011). At a global scale, climate fluctuations are identified within the Campanian-Maastrichtian interval, with a warming episode evidenced in benthic foraminifera $\delta^{18}O$, in TEX86, and in planktonic foraminifera during the mid-late Campanian (Friedrich et al., 2012; Linnert et al., 2014; Falzoni et al., 2016: Fig. 6). These climate fluctuations may have modified to some extent the hydrological cycle and changed the local hydrolysing conditions in the vicinity of the Zagros Basin. Such changes in sea-surface temperatures of the central part of the Zagros Basin are also suggested from calcareous nannofossil assemblages (Razmjooei et al., 2020b).

Variations in detrital sources are also susceptible to drive changes in clay mineralogical assemblages through time (Fig. 6). The main geodynamical evolution evident in this area is the 5,000 km long obduction-driven orogeny that affected the southern Tethyan margin from Lybia to Oman, linked to Africa-Eurasia convergence during the Late Cretaceous (Agard et al., 2011; Şengör and Stock, 2014). On both sides of the intra-oceanic subduction zone in the Zagros area, two ophiolitic belts were obducted, parallel to the south-western part of Iran. These complete ophiolites sequences contain well-preserved mantellic (harzburgite) and crustal (gabbro and basalt) rocks (Shafaii Moghadam and Stern, 2011).

Because of their mineralogical composition, oceanic crust rocks are very sensitive to chemical weathering, and plagioclase feldspar (basalt and gabbro's major components) degradation could provide the aluminum required to form kaolinite, incorporated in lateritic profiles widespread at low latitudes (Schopka et al., 2011; Giorgis et al., 2014). Illite and chlorite are primary minerals deriving from weathering and erosion of felsic, chlorite and mica-rich metamorphic rocks from the basement.

However, if the evolution of clay assemblages along the Late Cretaceous Shahneshin section was controlled by changes in the nature and provenance of the weathered and eroded rocks as sediment sources, a co-variation of kaolinite proportions with Ni/Al and Cr/Al ratios would be expected, that is not observed here (Fig. 6). Indeed, mafic and ultramafic rocks are notably concentrated in Ni and Cr (Azizi et al., 2015; MacKay and Ansdell, 2013), and detrital material eroded from such rocks and deposited nearby is expected to be enriched in Ni and Cr compared to material derived from weathering of crystalline basement. On the contrary, bulk rock Cr/Al and Ni/Al evolution along the section appears to be decoupled from the evolution in kaolinite proportions. The Cr/Al and Ni/Al ratios both display a sharp increase in the middle and late Campanian followed by a milder increase in the Maastrichtian, while kaolinite proportions decrease to values close to zero at the end of the late Campanian and remain close to zero afterwards, after the ca. 2Myr hiatus.

The evolution of Ni and Cr concentrations in the sediments do not support a change in the source of the detrital material as the main driver of clay mineral assemblage evolution in the studied section, between an ophiolite source generating kaolinite and a crystalline basement source generating illite and chlorite. More likely, evolution of clay mineral assemblages is controlled by changes in hydrolysing conditions in the studied area, with kaolinite-rich intervals reflecting more humid conditions and illite and chlorite-rich intervals reflecting drier conditions. The increase in Ni/Al and Cr/Al ratios from the middle Campanian

to the Maastrichtian may either mark the initiation of ophiolite weathering in this region, or of the weathering of the ultramafic, mantellic part of the ophiolite sequence that is over 10 times more enriched in Ni and Cr than the overlying basalt and gabbros (Azizi et al., 2013; Shafaii Moghadam and Stern, 2015; Nouri et al., 2019; Monsef et al., 2018). Weathering of mafic and ultramafic rocks can also provide the high magnesium content required to form chlorite and vermiculitic clays at the expense of smectites.

5.3. Evolution of the insoluble fraction $\varepsilon_{Nd(t)}$: insights on ophiolite weathering in Iran?

Detrital particles derived from the weathering and erosion of the bedrock retain the initial Nd isotope signature of the source rock (Goldstein et al., 1984). The Nd isotope signature of the detrital fraction recovered from marine sediments has thus been widely used to track sediment provenance (*e.g.* Frank et al., 2002; Goldstein and Hemming, 2003; Revel et al., 2010; van der Lubbe et al., 2016). Mantellic material, characterized by high Sm/Nd ratios, yield high ε_{Nd} values reflecting a radiogenic composition, while ancient crustal material, characterized by lower Sm/Nd ratios, yield negative ε_{Nd} values reflecting an unradiogenic composition.

The insoluble fraction analyzed in this work represents the residue obtained after removal of carbonates, Fe-Mn oxides, and organic matter from bulk sediment samples using acetic acid, hydroxyl-ammonium hydrochloride, and hydrogen peroxide respectively (Fig. 6, *see the Material and Method part*). In distal oceanic sites, authigenic clays can in some case contribute significantly to the insoluble fraction of the sediments which in that case may partly integrate the Nd isotope composition of bottom seawater (Chamley and Bonnot-Courtois, 1981; Dubinin, 2004; Karpoff et al., 2007). At Shahneshin, the sediments have been deposited in a bathyal environment within an oceanic channel during the Late Cretaceous (Fig. 1), relatively close to the continent. This proximity to land masses is also highlighted by the quite high sedimentation rate recorded throughout the section (Razmjooei et al., 2018;

Suppl. Fig. 1). Therefore, we think it unlikely for authigenic clays to represent a significant part of the insoluble fraction, and interpret the $\varepsilon_{Nd(t)}$ of this fraction as mostly reflecting the Nd isotope composition of local detrital inputs (Fig. 6). This view is supported by the REE pattern of the residue that is quite different from that of seawater characterized by a negative Ce anomaly, by depletion in light REE and enrichment in heavy REE (Fig. 5).

The decrease in $\varepsilon_{Nd(t)}$ of the detrital fraction during the sharp rise in Ni/Al and Cr/Al ratios recorded in the middle Campanian to Maastrichtian interval argues against an initiation of ophiolite weathering at that time, that should rather be associated by a large increase in $\varepsilon_{Nd(t)}$ values. The Nd isotope data rather support weathering of the mantellic ultramafic material (mantellic rocks) underlying basalt and gabbro (volcanic and crustal rocks) of the ophiolite sequence as a driver for the observed increase in Ni/Al and Cr/Al ratios. Ultramafic peridotites are much more enriched in Ni and Cr (Azizi et al., 2013; Shafaii Moghadam et al., 2014; Monsef et al., 2018; Nouri et al., 2019) but are not expected to markedly increase the $\varepsilon_{Nd(t)}$ value of detrital material (Blusztein et al., 1995), compared to that derived from the weathering of the overlying basalt and gabbros of the ophiolite sequence. If this interpretation is correct, our data then imply that ophiolite weathering was already initiated in the vicinity of the Zagros region during the Coniacian, at the base of the section, at least for the upper parts of the ophiolite sequences.

The decrease in Nd isotope values of the detrital fraction recorded from the middle Campanian to the Maastrichtian requires however the existence of an increasing input of an additional material with an unradiogenic composition (Fig. 6). The Nd isotope composition of the detrital fraction, in the range of -9 to -6 ε-units, actually appears quite unradiogenic all along the section considering the age and nature of the potentially exposed terranes in the vicinity of the Zagros Basin at that time, that are expected to deliver detrital material with a more radiogenic composition. The Nd isotope composition of obducted ophiolites both in the

Outer and Inner Zagros Ophiolitic Belts is radiogenic, with $\varepsilon_{Nd(t)}$ values at 80 Ma in the range of +4.9 to +9.8 ε-units (Shafaii Moghadam et al., 2012; Azizi et al., 2013; Shafaii Moghadam et al., 2014). Granitoid bodies formed prior to the Late Cretaceous and outcropping at present in Iran also tend to present relatively radiogenic ε_{Nd} values (*e.g.* -3.5 to -2.9 ε-units calculated at 80 Ma for the Tuyeh-Darvar Granitoid, Naderi et al., 2018, Suppl. Table 1; or -4 to +1.2 ε-units at 80 Ma for the granitoid body of the Misho region in northwest Iran, although two samples yield more unradiogenic values of -6.4 and -9.7 ε-units; Ahankoub et al., 2013, Fig. 7; Suppl. Table 1).

The relatively low ε_{Nd} values of the insoluble fraction, down to -9 ε-units, thus require mixing with an additional, unradiogenic source, with inputs that could have varied along the section. In a recent study, Nouri et al. (2019) has shown that some parts of the Harsin-Sahneh serpentinized peridotites in the mantle sequence of the Zagros ophiolite complex, exposed along the Zagros suture zone in western Iran, yield more unradiogenic values, down to -7.8 ε-units at 80 Ma (Fig. 7; Suppl. Table 1). These low values have been interpreted by these authors as reflecting interaction of peridotites with seawater during metasomatism in a supra-subduction zone system. Alteration of serpentinized peridotites may have partly contributed to the relatively low $\varepsilon_{Nd(t)}$ values observed in the insoluble fraction of Shahneshin. Other sources of unradiogenic material, farther away from the studied area, are the Khida terrane within the Arabian Shield, or the East Saharan Craton on the other side of the modern Red Sea. The Arabian-Nubian Shield, that represents the closest area with unradiogenic material, is composed of amalgamated juvenile oceanic arc terranes and ophiolite remnants, and of reworked older crust and metasediments in the flanks of the shield, that formed the suture between East and West Gondwana (Stern, 1994; Stein and Goldstein, 1996; Whitehouse et al., 1998, 2001; Stern, 2002; Kusky and Li, 2003). The juvenile oceanic arc terranes and ophiolite remnants, that compose the largest part of the shield, have ε_{Nd} values calculated at

80Ma typically between -5 to +18 ε-units (Duyverman et al., 1982; Johnson and Woldehaimanot, 2003; Stoeser and Frost, 2006; Fig. 7; Suppl. Table 1). On the western flank of the shield, a mix of juvenile and more ancient crust yield more variable and less radiogenic ε_{Nd} values, down to -35 ε-unit at 80Ma (Harms et al., 1990, 1994; Stern, 1994; Johnson and Woldehaimanot, 2003). The Khida terrane, that represents a small portion of a more ancient continental crust, outcrops at present in the eastern part of the shield and yields the most unradiogenic Nd isotope values of the Arabian Shield (ε_{Nd} values calculated at 80Ma ranging between -23.8 and -6.3 ε-units; Fig. 7; Suppl. Table 1). Although quite far away from the studied section, detrital material derived from these unradiogenic parts of the Arabian-Nubian Shield may have been brought by rivers, in proportions that could have evolved in the context of Africa-Eurasia convergence and associated tectonic movements, susceptible to modify river catchment areas.

Interestingly, variations in detrital fraction $\varepsilon_{Nd(t)}$ present a striking temporal coincidence with the evolution of clay mineralogical assemblages. More radiogenic $\varepsilon_{Nd(t)}$ values are recorded in the intervals rich in kaolinite while unradiogenic values are recorded during intervals devoid of kaolinite and rich in chlorite and illite (Fig. 6). Wind-blown dust can contribute significantly to the Nd isotope composition of the detrital material deposited in oceanic basins (Grousset et al., 1988; Grousset and Biscaye, 2005). Along the western African margin, markedly lower ε_{Nd} values (by up to +4 ε-units) have been recorded in the detrital fraction of deep-sea core sediments deposited during the drier last glacial maximum, compared to present-day values measured in core-tops at the same sites (Grousset et al., 1988). These authors have interpreted these more unradiogenic values as deriving from increasing inputs of Saharan wind-blown dust at these off-shore sites during the overall drier climate interval corresponding to the Last Glacial Maximum. Similarly, the relatively unradiogenic ε_{Nd} values recorded in the detrital fraction at Shahneshin may reflect to some

extent the presence of unradiogenic wind-blown dust mixed with radiogenic detrital material derived from the weathering of nearby ophiolites and granitoids. The origin of this unradiogenic dust would be difficult to determine, as it would be dependent of both atmospheric circulation and of the location of deserts on ancient continental crust, but it may have come from the East Saharan Craton, the Khida terrane, or, given the likely position of the site relative to the trade-winds, from the Eurasian craton as much of south-east Asia is thought to have been very dry during the late Cretaceous (Hasegawa et al., 2012). If this interpretation is correct, then the co-variations of kaolinite proportions in clay mineral assemblages with the ε_{Nd} values of the insoluble fraction would derive from significant variations in the contribution of this unradiogenic dust material. This contribution would have been higher in drier intervals marked by higher proportions of illite and chlorite, and lower in more humid intervals marked by higher proportions of kaolinite. The marked decrease in Nd isotope values of the insoluble fraction from the middle Campanian to the Maastrichtian, associated with high proportions of illite and chlorite, could thus reflect drier climatic conditions and an increased contribution of wind-blown unradiogenic material to the sediments of the section at that time.

5.4. An oceanic signal partially preserved?

The carbonate leachates all present a REE pattern typical of non-skeletal marine carbonates formed in shallow oxic seawater, with a negative Ce anomaly, a positive La anomaly, and an enrichment in heavy rare earth elements (Webb and Kamber, 2000; Tostevin et al., 2016). These REE patterns along with the significant difference, from 2 to over 4 ε-units recorded between the carbonate leachate and the residues ε_{Nd}, strongly suggest that the carbonate leachates record the ε_{Nd} of the local bottom seawater at Shahneshin.

It has been shown that on continental margins and proximal settings, local bottom seawater ε_{Nd} can be impacted by local detrital inputs, through processes called boundary

exchanges (Lacan and Jeandel, 2001; Jeandel, 2016). Therefore, in such settings, the evolution of local seawater ε_{Nd} can be governed by changes in the source of the material eroded nearby. At Shahneshin, variations in local bottom seawater ε_{Nd} mirror that of the detrital fraction from the Coniacian to the middle Campanian. This co-variation strongly suggests that changes in the Nd isotope composition of the sediments transported to the Zagros Basin have likely driven the Nd isotope composition of the local seawater during this interval. By contrast, a decoupling of both isotopic signals is depicted from the late Campanian onward, highlighted by the increasing difference recorded between $\varepsilon_{Nd(t)bottom}$ $_{seawater}$ and $\varepsilon_{Nd(t)insoluble\ residue}$ from about 2 to over 4 ε-units ($\Delta\varepsilon_{Nd(t)\ boot.\ Sweater\ -\ insol\ resi}$; Fig. 6). While the $\varepsilon_{Nd(t)}$ of the residue displays a marked decrease of about 3 ε-units from the middle Campanian to the late Maastrichtian, the $\varepsilon_{Nd(t)}$ of the local bottom waters only shows a mild decrease of less than 1 ε-unit on average. This difference points to increasing inputs of a radiogenic water mass in the Zagros Basin during this interval, driving the Nd isotope composition of the local seawater further away from the unradiogenic composition of the nearby detrital supply. At that time, the only deep or intermediate water masses reported in the literature with radiogenic compositions above -5 ε-units are water masses from the Pacific Ocean ($\varepsilon_{Nd(t)}$ ranging between -7 and -3 ε-units during the Late Cretaceous; Thomas, 2004; Hague et al., 2012; Thomas et al., 2014; Moiroud et al., 2016; Haynes et al., 2020).

During the Late Cretaceous, the large wind-driven westward flowing TCC flowed all around the globe at low latitudes, from the Indian and Pacific Oceans into the Atlantic Ocean through the Tethys, and then back to the Pacific through the Caribbean seaway (Winterer, 1991; Föllmi and Delamette, 1991; Otto-Bliesner et al., 2002; Donnadieu et al., 2006). The development of upwellings along the southern Tethyan margin during the Campanian and Maastrichtian, inferred from high productivity assemblages as radiolarites orrganic-matter layers, and the occurrence of large phosphorite deposits (Salaj and Nairn, 1987 ; Föllmi et al.,

1992 ; Almogi-Labin et al., 1993 ; Pufahl et al., 2003 ; Lüning et al., 1998 ; Meilijson et al., 2014 ; El-Shafeiy et al., 2014 ; Bou Daher et al., 2014, 2015), has been linked to an intensification of the TCC at that time (Pucéat et al., 2005; Soudry et al., 2004, 2006). Our new results thus support a more intense TCC in the late Campanian to Maastrichtian interval, that would have resulted in enhanced inputs of radiogenic Pacific waters into the Zagros Basin, driving the $\varepsilon_{Nd(t)}$ of the local seawater further away from that of the more unradiogenic detrital inputs. Our work additionally suggests that the TCC could have extended to bathyal depths during the Late Cretaceous, at least within the Zagros Basin.

Our results also highlight the quite radiogenic composition of bathyal waters in the Zagros Basin, that display $\varepsilon_{Nd(t)}$ values in the range of -3.5 to -5.5 ε-units, about 2 to 3 ε-units above the $\varepsilon_{Nd(t)}$ values of shallow waters of the Negev (Soudry et al., 2004, 2006). If such a radiogenic composition is confirmed as a feature of bathyal waters in the eastern Tethys, the development of an intense upwelling system could then have contributed to the increase in shallow water $\varepsilon_{Nd(t)}$ values recorded in the Negev from the Turonian to the Campanian (Soudry et al., 2004; 2006), along with the intensification of the TCC. More data from other bathyal sites in the Tethys are however required to confirm the latter hypothesis.

6. Conclusions

Our new clay mineralogical data coupled to sediment Ni/Al and Cr/Al ratios suggest that the clay sedimentation of the eastern Tethys Shahneshin section was mainly driven by changes in local hydrolysing conditions, potentially linked to global climatic change as suggested by global records in benthic foraminifer $\delta^{18}O$. Humid intervals in the Coniacian to Santonian and middle Campanian to early late Campanian periods could have favoured kaolinite formation while more arid intervals (early Campanian and latest Campanian to late Maastrichtian) would have inhibited kaolinite formation and promoted a higher proportion of illite and chlorite in clay mineral assemblages.

The large increase recorded in sediment Ni/Al and Cr/Al from the upper Campanian onward, that is not associated to a concomitant increase in the $\varepsilon_{Nd(t)}$ of the detrital fraction, is interpreted as reflecting the alteration and erosion of the mantellic ultramafic material of the ophiolite sequence, that underlies basalt and gabbro. Following this interpretation, our data set imply that the ophiolite sequence was exposed to continental alteration and erosion in this area as soon as the Coniacian. Our results thus support a possible role of ophiolite obduction along the southern Tethyan margin in the Late Cretaceous long-term cooling through weathering of the exposed material, a process that draws down atmospheric CO_2.

The increasing difference recorded between the $\varepsilon_{Nd(t)}$ of the local bottom seawater and of the residue from the middle Campanian to the Maastrichtian points to a growing influence of a radiogenic water mass entering the Zagros Basin during this period. These results support an intensification of the westward flowing TCC during the Campanian and Maastrichtian that would have brought larger fluxes of radiogenic Pacific waters into the eastern Tethys. Our new data suggest that the TCC would have extended down to bathyal depth at that time, at least in the Zagros Basin. They also provide the first $\varepsilon_{Nd(t)}$ values of intermediate to deep waters within the Tethyan area, revealing quite radiogenic values in this part of the eastern Tethys, in the range of -3.5 to -5.5 ε-units. Upwelling of such radiogenic waters onto the Negev platform during the Campanian and Maastrichtian could have partly contributed to the recorded increase in local seawater $\varepsilon_{Nd(t)}$ values at that time.

Acknowledgements

References

Adatte, T., Keller, G., Stinnesbeck, W., 2002. Late Cretaceous to early Paleocene climate and sea-level fluctuations: the Tunisian record. *Palaeogeogr. Palaeoclimatol. Palaeoecol. 178*, 165–196.

Agar, R. A., Stacey, J.S., Whitehouse, M. J., 1992. Evolution of the southern Afif Terrane - a geochronological study. *Saudi Arabian Directorate General of Mineral Resources*, 10–15.

Agard, P., Omrani, J., Jolivet, L., Mouthereau, F., 2005. Convergence history across Zagros (Iran): constraints from collisional and earlier deformation *Int. J. Earth Sci. 94*, 401–419.

Agard, P., Omrani, J., Jolivet, L., Whitechurch, H., Vrielynck, B., Spakman, W., Monié, P., Meyer, B., Wortel, R., 2011. Zagros orogeny: a subduction-dominated process. *Geol. Mag. 148*, 692–725.

Ahankoub, M., Jahangiri, A., Asahara, Y., Moayyed, M., 2013. Petrochemical and Sr-Nd isotope investigations of A-type granites in the east of Misho, NW Iran. *Ara.b J. Geosci. 6*, 4833–4849.Ala, M.A., Kinghorn, R.R.F., Rahman, M.T., 1980. Organic geochemistry and source rock characteristics of he Zagros petroleum province, southwest Iran. *J. Pet. Geol. 3*, 61–89.

Alavi, M., 1980. Tectonostratigraphic evolution of the Zagrosides of Iran. *Geology 8*, 144–149.

Alavi, M., 1994. Tectonics of the Zagros orogenic belt of Iran: new data and interpretations. *Tectonophysics 229*, 211–238.

Almogi-Labin, A., Bein, A., Sass, E., 1993. Late Cretaceous upwelling system along the southern Tethys margin (Israel): interrelationship between productivity, bottom water environments, and organic matter preservation. *Paleoceanography 8*, 671–690.

Alsenz, H., Regnery, J., Ashckenazi-Polivoda, S., Meilijson, A., Ron-Yankovich, L., Abramovich, S., Illner, P., Almogi-Labin, A., Feinstein, S., Berner, Z., 2013. Sea surface

temperature record of a Late Cretaceous tropical southern Tethys upwelling system. *Palaeogeogr. Palaeoclimatol. Palaeoecol. 392*, 350–358.Ashckenazi-Polivoda, S., Abramovich, S., Almogi-Labin, A., Schneider-Mor, A., Feinstein, S., Püttmann, W., Berner, Z., 2011. Paleoenvironments of the latest Cretaceous oil shale sequence, Southern Tethys, Israel, as an integral part of the prevailing upwelling system. *Palaeogeogr. Palaeoclimatol. Palaeoecol. 305*, 93–108.

Ao, S., Xiao, W., Khalatbari Jafari, M., Talebian, M., Chen, L., Wan, B., Ji, W., Zhang, Z., 2016. U–Pb zircon ages, field geology and geochemistry of the Kermanshah ophiolite (Iran): From continental rifting at 79 Ma to oceanic core complex at ca. 36 Ma in the southern Neo-Tethys. *Gondw. Research. 31*, 305–318.

Azizi, H., Hadi, A., Asahara, Y., Mohammad, Y.O., 2013. Geochemistry and geodynamics of the Mawat mafic complex in the Zagros Suture zone, northeast Iraq. Central European *J. of Geosci. 5*, 523–537.

Babaie, H., Babaei, A., Ghazi, A.M., Arvin, M., 2006. Geochemical, $^{40}Ar/^{39}Ar$ age, and isotopic data for crustal rocks of the Neyriz ophiolite, Iran. *Canad. J. Earth Sci. 43*, 57–70.

Bárdossy, G., Dercourt, J., 1990. Les gisements de bauxites téthysiens (Méditerranée, Proche et Moyen Orient); cadre paléogéographique et contrôles génétiques. *Bull. Soc. Géol. France 6*, 869–888.

Barrat, J. A., Keller, F., Amossé, J., Taylor, R. N., Nesbitt, R. W., Hirata, T., 1996. Determination of rare earth elements in sixteen silicate reference samples by ICP-MS after Tm addition and ion exchange separation. *Geostandards News. 20*, 133–139.

Barrier, E., Vrielynck, B., 2007. Early Campanian (83 – 80.5 Ma). *In*: Palaeotectonic maps of the Middle East, Atlas of maps; Tectono-Sedimentary-Palinspastic maps from Late Norian to Pliocene. *Commission for the Geological Map of the World*, Paris.

Bayon, G., German, C.R., Boella, R.M., Milton, J.A., Taylor, R.N., Nesbitt, R.W., 2002. An

improved method for extracting marine sediment fractions and its application to Sr and Nd isotopic analysis. *Chem. Geol. 187*, 179–199.

Bayon, G., Barrat, J.A., Etoubleau, J., Benoit, M., Bollinger, C., Révillon, S., 2009. Determination of rare earth elements, Sc, Y, Zr, Ba, Hf and Th in geological samples by ICP-MS after Tm addition and alkaline fusion. *Geostand. Geoanalyt. Research 33*, 51–62.

Bayon, G., Dennielou, B., Etoubleau, J., Ponzevera, E., Toucanne, S., Bermell, S., 2012. Intensifying weathering and land use in iron age Central Africa. *Science 335*, 1219–1222.

Beaufort, D., Rigault, C., Billon, S., Billault, V., Inoue, A., Inoue, S., Patrier, P. 2015. Chlorite and chloritization processes through mixed-layer mineral series in lowtemperature geological systems – a review. *Clay minerals 50*, 491-523.

Be'eri-Shlevin, Y., Katzir, Y., Blichert-Toft, J., Kleinhanns, I. C., Whitehouse, M. J., 2010. Nd–Sr–Hf–O isotope provinciality in the northernmost Arabian–Nubian Shield: implications for crustal evolution. *Contributions to Mineralogy and Petrology 160*, 181–201.

Berberian, M., King, G.C.P., 1981. Towards a paleogeography and tectonic evolution of Iran. *Canad. J. Earth Sci. 18*, 210-265.

Begemann, F., Kenneth, R.L., Lugmair, G.W., Walker, R.J., 2001. Call for improved set of decay consants for geochronological use. *Geochim. Cosmochim. Acta 65*, 111–121. Blusztajn, J., Hart, S.R., Shimizu, N., McGuire, A.V., 1995. Trace-element and isotopic characteristics of spinel peridotite xenoliths from Saudi Arabia. *Chemi. Geol. 123*, 53-65.Bokhari, F.Y., Kramers, J.D., 1981. Island-arc character and late Precambrian age of volcanics at Wadi Shwas, Hijaz, Saudi Arabia: geochemical and Sr and Nd isotopic evidence. *Earth Planet. Sci. Lett. 54*, 409–422.

Bornemann, A., Norris, R.D., Friedrich, O., Beckmann, B., Schouten, S., Sinninghe Damsté J.S., Vogel, J., Hofmann, P., Wagner, T., 2008. Isotopic Evidence for Glaciation During

the Cretaceous Supergreenhouse. *Science 319*, 189–192.

Bosworth, W., Guiraud, R., Kessler, L.G., 1999. Late Cretaceous (ca. 84 Ma) compressive deformation of the stable platform of northeast Africa (Egypt): Far-field stress effects of the "Santonian event" and origin of the Syrian arc deformation belt. *Geology 27*, 633–636.

Bou Daher, S., Nader, F.H., Strauss, H., Littke, R., 2014. Depositional environment and source-rock characterisation of organic-matter rich Upper Santonian–Upper Campanian carbonates, northern Lebanon. *J. Petrol. Geol. 37*, 5–24.

Bou Daher, S.B., Nader, F.H., Müller, C., Littke, R., 2015. Geochemical and petrographic characterization of Campanian–Lower Maastrichtian calcareous petroleum source rocks of Hasbayya, South Lebanon. *Mar. Petrol. Geol. 64*, 304–323.Bouvier, A., Vervoort, J.D., Patchett, P.J., 2008. The Lu–Hf and Sm–Nd isotopic composition of CHUR: constraints from unequilibrated chondrites and implications for the bulk composition of terrestrial planets. *Earth Planet. Sci. Lett. 273*, 48–57.

Carignan, J., Hild, P., Mevelle, G., Morel, J., Yeghicheyan, D., 2001. Routine analyses of trace elements in geological samples using flow injection and low pressure on-line liquid chromatography coupled to ICP-MS: a study of geochemical reference materials BR, DR-N, UB-N, AN-G and GH. *Geostandards Newsletter 25*, 187–198.

Chamley, H., 1989. Clay Sedimentology. Springer. Berlin, 623 pp.

Chamley, H., Bonnot-Courtois, C., 1981. Argiles authigènes et terrigènes de l'Atlantique et du Pacifique. NW. *Oceanol. Acta 4*, 229–238.

Chamley, H., Deconinck, J-F., Millot, G., 1990. Sur l'abondance des minéraux smectitiques dans les sédiments marins communs déposés lors des périodes de haut niveau marin du Jurassique supérieur au Paléogène. *C R. Acad. Sci. Paris, Ser. II 311*, 1529–1536.

Chauvel., C., Blichert-Toft, J., 2001. A hafnium isotope and trace element perspective on melting of the depleted mantle. *Earth Planet. Sci. Lett. 190*, 137–151.

Chenot, E., Pellenard, P., Martinez, M., Deconinck, J.-F., Amiotte-Suchet, P., Thibault, N., Bruneau, L., Cocquerez, T., Laffont, R., Pucéat, E., Robaszynski, F., 2016. Clay mineralogical and geochemical expressions of the "Late Campanian Event" in the Aquitaine and Paris basins (France): Palaeoenvironmental implications. *Palaeogeogr. Palaeoclimatol. Palaeoecol. 447*, 42–52.

Chenot, E., Deconinck, J-F., Pucéat, E., Pellenard, P., Guiraud, M., Jaubert, M., Jarvis, I., Thibault, N., Cocquerez, T., Bruneau, L., Razmjooei, M.J., Boussaha, M., Richard, J., Sizun, J-P., Stemmerik, L., 2018. Continental weathering as a driver of Late Cretaceous cooling: new insights from clay mineralogy of Campanian sediments from the southern Tethyan margin to the Boreal realm, *Global Planet. Change 162*, 292–312.

Claesson, S., Pallister, J.S., Tatasumoto, M., 1984. Samarium-neodymium data on two late Proterozoic ophiolites of Saudi Arabia and implications for crustal and mantle evolution. *Contributions to Mineralogy and Petrology 85*, 244–252.

Cogné, J.-P., Humler, E., 2006. Trends and rhythms in global seafloor generation rate. *Geochem. Geophys. Geosys. 7*, 1–17.

Darabi, G., Moghaddam, I.M., Sadeghi, A., Yusefi, B., 2018. Planktonic foraminifera and sea-level changes in the upper Cretaceous of the Gurpi Formation, Lorestan basin, SW Iran. *J. Afr. Earth Sci. 38*, 201–218.

Deconinck, J.-F., Chamley, H., 1995. Diversity of smectite origins in the Late Cretaceous sediments: example of chalks from northern France. *Clay Miner. 30*, 365–380.

Delaloye, M., Desmons, J., 1980. Ophiolites and melange terranes in Iran: a geochronological study and its paleotectonic implications. *Tectonophysics 68*, 83–111.

Dercourt, J., Zonenshain, L.P., Ricou, L.-E., Kazmin, V.G., Le Pichon, X., Knipper, A.L., Grandjacquet, C., Sbortshikov, I.M., Geyssant, J., Lepvrier, C., Pechersky, D.H., Boulin, J., Sibuet, J.-C., Savostin, L.A., Sorokhtin, O., Westphal, M., Bazhenov, M.L., Lauer, J.P.,

Biju-Duval, B., 1986. Geological evolution of the tethys belt from the atlantic to the pamirs since the LIAS. *Tectonophysics 123*, 241–315.

Donnadieu, Y., Goddéris, Y., Pierrehumbert, R., Dromart, G., Fluteau, F., Jacob, R., 2006. A GEOCLIM simulation of climatic and biogeochemical consequences of Pangea breakup. *Geochem. Geophy. Geosys. 7*, 1–21.

Dubinin, A.V., 2004. Geochemistry of rare earth elements in the ocean. *Lithology and mineral resources 39*, 289–307.

Duyverman, H.J., Harris, N.B.W., Hawkesworth, C.J., 1982. Crustal accretion in the Pan African: Nd and Sr isotope evidence from the Arabian Shield. *Earth Planet. Sci. Lett.* 59, 315–326.

El-Shafeiy, M., Birgel, D., El-Kammar, A., El-Barkooky, A., Wagreich, M., Mohamed, O., Peckmann, J., 2014. Palaeoecological and post-depositional changes recorded in Campanian–Maastrichtian black shales, Abu Tartur plateau, Egypt. *Cret. Res. 50*, 38–51.

Eshet, Y., Almogi-Labin, A., 1996. Calcareous nannofossils as paleoproductivity indicators in Upper Cretaceous organic-rich sequences in Israel. *Marine Micropal. 29*, 37–61.

Falzoni, F., Petrizzo, M.-R., Clarke, L.J., Macleod, K.G., Jenkyns, H.C., 2016. Long-term Late Cretaceous oxygen- and carbon-isotope trends and planktonic foraminiferal turnover: A new record from the southern midlatitudes. *GSA Bulletin 128*, 1725–1735.

Föllmi, K., B., Delamette, M., 1991. Model simulation of Mid-Cretaceous Ocean Circulation. *Science 251*, pp. 94.

Föllmi, K.B., Garrison, R.E., Ramirez, P.C., Zambrano-Ortiz, F., Kennedy, W.J., Lehner, B.L., 1992. Cyclic phosphate-rich successions in the upper Cretaceous of Colombia. *Palaeogeogr. Palaeoclimatol. Palaeoecol. 93*, 151–182.

Frank, M., Whiteley, N., Kasten, S., Hein, J.R., O'Nions, K., 2002. North Atlantic Deep

Water export to the Southern Ocean over the past 14 Myr: Evidence from Nd and Pb isotopes in ferromanganese crusts. *Paleoceanography 17,* 12-1–12-9.

Franks, P.J., Royer, D.L., Beerling, D.J., Van de Water, P.K., Cantrill, D.J., Barbour, M.M., Berry, J.A., 2014. New constraints on atmospheric CO_2 concentration for the Phanerozoic. *Geophy. Res. Letters 41*, 4685–4694.

Friedrich, O., Norris, R.D., Erbacher, J., 2012. Evolution of middle to Late Cretaceous oceans—A 55 my record of Earth's temperature and carbon cycle. *Geology 40*, 107–110.

Ghasemi, H., Juteau, T., Bellon, H., Sabzehi, M., Whitechurch, H., Ricou, L.E., 2002. The mafic-ultramafic complex of Sikhoran (central Iran): a polygenetic ophiolite complex. *C. R. Geosci. 334*, 431–438.

Giorgis, I., Bonetto, S., Giustetto, R., Lawane, A., Pantet, A., Rossetti, P., Thomassin, J.H., Vinai, R., 2014. The lateritic profile of Balkouin, Burkina Faso: Geochemistry, mineralogy and genesis. *J. African. Earth Sciences. 90,* 31–48.

Goldstein, S.L., Hemming, S.R., 2003. Long-lived Isotopic Tracers in Oceanography, Paleoceanography, and Ice-sheet Dynamics. *Treatise on Geochemistry 6*, 453–489.

Goldstein, S.L., O'Nions, R.K., Hamilton, P.J., 1984. A Sm-Nd isotopic study of atmospheric dusts and particulates from major river systems. *Earth Planet. Sci. Lett. 70*, 221–236.

Govindaraju, K., 1995. 1995 working values with confidence limits for twenty-six CRPG, ANRT and IWG-GIT geostandards. *Geostandards Newsletter 19*, 1–32.

Gradstein, F.M., Ogg, J.G., Schmitz, M., Ogg, G., 2012. The Geologic Time Scale 2012. Elsevier, pp. 1176.

Grousset, F.E., Biscaye, P.E., 2005. Tracing dust sources and transport patterns using Sr, Nd and Pb isotopes. *Chemi. Geol. 222*, 149–167.

Grousset, F.E., Biscaye, P.E., Zindler, A., Prospero, J., Chester, R., 1988. Neodymium

isotopes as tracers in marine sediments and aerosols: North Atlantic. *Earth Planet. Sci. Lett. 87*, 367–378.

Guiraud, R., Bosworth, W., 1997. Senonian basin inversion and rejuvenation of rifting in Africa and Arabia: synthesis and implications to plate-scale tectonics. *Tectonophysics 282*, 39–82.

Hague, A.M., Thomas, D.J., Huber, M., Korty, R., Woodard, S.C., Jones, L.B., 2012. Convection of North Pacific deep water during the early Cenozoic. *Geology 40*, 527–530.

Harms, U., Schandelmeier, H., Darbyshire, D.P.F., 1990. Pan-African reworked early/middle Proterozoic crust in NE Africa west of the Nile: Sr and Nd isotope evidence. *J. of the Geological Soc. 147*, 859–872.

Harms, U., Darabyshire, D.P.F., Denkler, T., Hergot, M., Schandelmeier, H., 1994. Evolution of the Neoproterozoic Delgo Suture zone and crustal growth in the Northern Sudan: geochemical and radiogenic isotope constrains. *Geologische Rundschau 83*, 591–603.

Hasegawa, H., Tada, R., Jiang, X., Sugenuma, Y., Imsamut, S., Charusiri, P., Ichinnorov, N., Khand, Y., 2012. Drastic shrinking of the Hadley circulation during the mid-Cretaceous Supergreenhouse, Climate of the Past 8, 1323–1337.

Haynes, S.J., Macleod, K.G., Ladant, J.-B., Guchte, A.V., Rostami, M.A., Poulsen, C.J., Martin, E.E., 2020. Constraining sources and relative flow rates of bottom waters in the Late Cretaceous Pacific Ocean. *Geology 48*, 509–513.

Hegner, E., Pallister, J.S., 1989. Pb, Sr, and Nd isotopic characteristics of Tertiary Red Sea rift volcanics from the central Saudi Arabian coastal plain. *J. of Geophysical Research 94*, 7749–7755.

Hemmati-Nasab, M., Ghasemi-Nejad, E., Darvishzad, B., 2008. Paleobathymetry of the Gurpi Formation based on benthic and planktonic foraminifera in Southwestern Iran. *J Sci., Islamic Republic of Iran 34*, 157–173.

Homke, S., Verges, J., Serra-Kiel, J., Bernaola, G., Sharp, I., Garces, M., Montero-Verdu, I., Karpuz, R., Goodarzi, M.H., 2009. Late Cretaceous-Paleocene formation of the proto-Zagros foreland basin, Lurestan Province, SW Iran. *Geol. Soc. Am. Bull. 121*, 963–978.

Huber, B.T., Hodell, D.A., Hamilton, C.P., 1995. Middle-Late Cretaceous climate of the southern high latitudes: stable isotopic evidence for minimal equator-to-pole thermal gradients. *Geol. Soc. Am. Bull. 107,* 1164–1191.

Huber, B.T., Norris, R.D., Macleod, K.G., 2002. Deep-sea paleotemperature record of extreme warmth during the Cretaceous. *Geology 30*, 123–126.

Huber, B.T., Macleod, K.G., Watkins, D. K., Coffin, M.F., 2018. The rise and fall of the Cretaceous Hot Greenhouse climate. *Global Planet. Change 167*, 1–23.

Jagoutz, O., Macdonald, F.A., Royden, L., 2016. Low-latitude arc–continent collision as a driver for global cooling. *PNAS 113*, 4925–4940.

Jeandel, C., 2016. Overview of the mechanisms that could explain the « Boundary Exchange » at land-ocean contact. *Philosophical Transactions of the Royal Society A: Mathematical, Physical and Engineering Sciences 374*.

Jochum, K. P., Weis, U., Schwager, B., Stoll, B., Wilson, S.A., Haug, G.H., Andreae, M.O., Enzweiler, J., 2016. Reference values following ISO Guidelines for frequently requested rock reference materials. *Geostand. and Geoanal. Research 40*, 333–350.

Johnson, P.R., Woldehaimanot, B., 2003. Development of the Arabian-Nubian Shield: perspectives on accretion and deformation in the northern East African Orogen and the assembly of Gondwana. *Geological Society, London, Special Publications 206*, 289–325.

Jolivet, L., Faccenna, C., Agard, P., Frizon de Lamotte, D., Menant, A., Sternai, P., Guillocheau, F., 2016. Neo-Tethys geodynamics and mantle convection: from extension to compression in Africa and a conceptual model for obduction. *Can. J. Earth Sci. 53*, 1190–1204.

Karpoff, A.M., Destrigneville, C., Stille, P., 2007. Clinoptilolite as a new proxy of enhanced biogenic silica productivity in lower Miocene carbonate sediments of the Bahamas platform: Isotopic and thermodynamic evidence. *Chem. Geol. 245*, 285–304.

Keller, G., Adatte, T., Burns, S. J., Tantawy, A.A., 2002. High-stress palaeoenvironnmeent during the late Maastrichtian to early Paleocene in Central Egypt. *Palaeogeogr. Palaeoclimatol. Palaeoecol. 187,* 35–60.

Koop, W.J., Stoneley, R., 1982. Subsidence history of the Middle East Zagros Basin. *Phil. Trans. Royal Soc. London 305*, 149–168.

Kröner, A., Linnebacher, P., Stern, R. J., Reischmann, T., Manton, W., Hussein, I. M., 1991. Evolution of Pan-African island arc assemblages in the southern Red Sea Hills, Sudan and in southwestern Arabia as exemplified by geochemistry and geochronology. *Precambrian Research 53*, 99–118.

Koster, D., Liegeois, J.-E, 2001. Sr, Nd isotopes and geochemistry of the Bayuda Desert high-grade metamorphic basement (Sudan): an early Pan-African oceanic convergent margin, not the edge of the East Saharan ghost craton? *Precambrian Research 109*, 1–23.

Kusky, T.M., Li, J., 2003. Paleoproterozoic tectonic evolution of the North China Craton. *J. of Asian Earth Sci 22,* 38. –397.

Lacan, F., Jeandel, C., 2001. Tracing Papua New Guinea imprint on the central Equatorial Pacific Ocean using neodymium isotopic compositions and Rare Earth Element patterns. *Earth Planet. Sci. Lett. 186*, 497–512.

Lanphere, M. A., Pamić, J., 1983. [40]Ar [39]Ar and tectonic setting of ophiolite from the Neyriz, southeast Zagros Range, Iran. *Tectonophysics 96*, 245–256.

Linnert, C., Robinson, S.A., Lees, J.A., Brown, P.R., Pérez-Rodríguez, I., Petrizzo, M.R., Falzoni, F., Littler, K., Arz, J.A., Russell, E.E., 2014. Evidence for global cooling in the Late Cretaceous. *Nat. Comm.*, 1–7.

Lugmair, G.W., Marti, K., 1977. Sm-Nd-Pu timepieces in the Angra dos Reis meteorite. *Earth Planet. Sci. Lett. 35,* 273–284.

Lüning, S., Marzouk, A.M., Morsi, A.M., Kuss, J., 1998. Sequence stratigraphy of the Upper Cretaceous of central-east Sinai, Egypt. *Cret.. Res. 19*, 153–195.

MacKay, C.B., Ansdell, K.M., 2013. Geochemical study of mafic and ultramafic rocks from southern Hall Peninsula, Baffin Island, Nunavut. *In* Summary of Activities 2013, *Canada-Nunavut Geoscience Office*, 85–92.

MacLeod, K.G., Londoño, C.I., Martin, E.E., Berrocoso, Á.., Basak, C., 2011. Changes in North Atlantic circulation at the end of the Cretaceous greenhouse interval. *Nat. Geosci. 4*, 779–782.

McKenzie, R., Horton, B.K., Loomis, S. E., Stockli, N.J., Planavsky, N.J., Lee, C.A., 2016. Continental arc volcanism as the principal driver of icehouse-greenhouse variability, *Science 352*, 444–447.

Meilijson, A., Ashckenazi-Polivoda, S., Ron-Yankovich, L., Illner, P., Alsenz, H., Speijer, R.P., Almogi-Labin, A., Feinstein, S., Berner, Z., Püttmann, W., Abramovich, S., 2014. Chronostratigraphy of the Upper Cretaceous high productivity sequence of the southern Tethys, Israel. *Cret.. Res. 70*, 187–213.

Mills, B.J.W., Krause, A.J., Scotese, C.R., Hill, D.J., Shields, G.A., Lenton, T.M., 2019. Modelling the long-term carbon cycle, atmospheric CO_2 and Earth surface temperature from late Neoproterozoic to present day. *Gondw. Res. 67*, 172–186.

Moghazi, A. M., Andersen, T., Oweiss, G. A., Elbouse1ly, A. M., 1998. Geochemical and Sr-Nd-Pb isotopic data bearing on the origin of Pan-African granitoids in the Kid area, southeast Sinai, Egypt. *J. Geol. Soc., London 155*, 697–710.

Moiroud, M., Martinez, M., Deconinck, J.-F., Monna, F., Pellenard, P., Riquier, L., Compagny, M., 2012. High-resolution clay mineralogy as a proxy for orbital tuning:

example of the Hauterivian-Baremian transition in the Beltic Cordillera (SE Sapin). *Sediment. Geol. 282*, 336–346.

Moiroud, M., Pucéat, E., Donnadieu, Y., Bayon, G., Guiraud, M., Voigt, S., Deconinck, J.-F., Monna, F., 2016. Evolution of neodymium isotopic signature of seawater during the Late Cretaceous: Implications for intermediate and deep circulation. *Gondw. Res. 36*, 503–522.

Moore, D.M., Reynolds, R.C., 1997. X-Ray diffraction and the identification and analysis of clay minerals, 2nd edition. (Eds.) Oxford University Press, Oxford, New York, pp. 378.

Monsef, I., Monsef, R., Mata, J., Zhang, Z., Pirouz, M., Rezaian, M., Esmaeili, R., Xiao, W., 2018. Evidence for an early-MORB to fore-arc evolution within the Zagros suture zone: Constraints from zircon U-Pb geochronology and geochemistry of the Neyriz ophiolite (South Iran). *Gondw. Res. 62*, 287–305.

Motiei, H., 1993. Stratigraphy of Zagros. Tehran: Geological Survey of Iran.

Murphy, D.P., Thomas, D.J., 2012. Cretaceous deep-water formation in the Indian sector of the Southern Ocean: Cretaceous Deep-Water Circulation. *Paleoceanography 27*, 1–12.

Murphy, D.P., Thomas, D.J., 2013. The evolution of Late Cretaceous deep-ocean circulation in the Atlantic basins: Neodymium isotope evidence from South Atlantic drill sites for tectonic controls: Cretaceous Atlantic Deep Circulation. *Geochem. Geophys. Geosyst. 14*, 5323–5340.

Naderi, A., Ghasemi, H., Santos, J.F., Rocha, F., Griffin, W.L., Shafaii Moghadam, H., Papadopoulou, L., 2018. Petrogenesis and tectonic setting of the Tuyeh-Darvar Granitoid (Northern Iran): Constraints from zircon U-Pb geochronology and Sr-Nd isotope geochemistry. *Lithos 318*, 494–508.

Nouri, F., Asahara, Y., Azizi, H., Tsuboi, M., 2019. Petrogenesis of the Harsin–Sahneh serpentinized peridotites along the Zagros suture zone, western Iran: new evidence for mantle metasomatism due to oceanic slab flux. *Geol. Magazine 156*, 772–800.

Notholt, A.J.G., 1985. Phosphate resources in the Mediterranean (Tethyan) phosphogenic province: a progress report. *Sci. Geol. Memoire 77*, 9–21.

O'Brien, C.L., Robinson, S.A., Pancost, R.D., Damsté, J.S.S., Schouten, S., Lunt, D.J., Alsenz, H., Bornemann, A., Bottini, C., Brassell, S.C., Farnsworth, A., Forster, A., Huber, B.T., Inglis, G., Jenkyns, H. C., Linnert, C., Littler, K., Markwick, P., McAnena, A., Mutterlose, J., Naafs, B.D.A., Püttmann, W., Sluijs, A., Van Helmond, N.A.G.M., Vellekoop, J., Wagner, T., Wrobel, N.E., 2017. Cretaceous sea-surface temperature evolution: Constraints from TEX86 and planktonic foraminiferal oxygen isotopes. *Earth Sci. Rev. 172*, 224–247.

Ogg, J.G., Ogg, G., Gradstein, F.M., 2016. A Concise Geologic Time Scale 2016. Elsevier. 250 pages.

Otto-Bliesner, B. L., Upchurch, G. R., 1997. Vegetation-induced warming of high latitude regions during the Late Cretaceous period. *Letters to nature 385*.

Otto-Bliesner, B.L., Brady, E.C., Shields, C., 2002. Late Cretaceous ocean: Coupled simulations with the National Center for Atmospheric Research climate system model. *J. of Geophy. Res.: Atmospheres 107*, ACL–11–14.

Petschick, R., 2000. MacDiff Ver. 4.2.6. Manual Geologisch-Palaontologisches Institute Johann Wolfgang Goethe Universitat Frankfurt Main senckenberganlage, 32–34.

Philip, J., Floquet, M., 2000. Early Campanian (83 – 80.5 Ma). *In:* Crasquin, S. (Coord.), Atlas Peri-Tethys, Palaeogeographic maps. Explanatory notes. *Commission for the Geol. Map of the World*, Paris, 145–152.

Pucéat, E., Lécuyer, C., Sheppard, S.M.F., Dromart, G., Reboulet, S., Grandjean, P., 2003. Thermal evolution of Cretaceous Tethyan marine waters inferred from oxygen isotope composition of fish tooth enamels. *Paleoceanography 18*, 1–12.

Pucéat, E., Lécuyer, C., Reisberg, L., 2005. Neodymium isotope evolution of NW Tethyan

upper ocean waters throughout the Cretaceous. *Earth Planet. Sci. Lett. 236*, 705–720.

Pufahl, P.K., Grimm, K.A., Abed, A.M., Sadaqah, R.M.Y., 2003. Upper Cretaceous (Campanian) phosphorites in Jordan: implications for the formation of a south Tethyan phosphorite giant. *Sediment. Geol. 161*, 175–205.

Razmjooei, M.J., Thibault, N., Kani, A., Mahanipour, A., Boussaha, M., Korte, C., 2014. Coniacian-Maastrichtian calcareous nannofossil biostratigraphy and carbon-isotope stratigraphy in the Zagros Basin (Iran): consequences for the correlation of the Late Cretaceous Stage Boundaries between the Tethyan and Boreal realms. *News. Stratigr. 47*, 183–209.

Razmjooei, M., Thibault, N., Kani, A., Dinarès-Turell, J., Pucéat, E., Shahriari, S., Radmacher, W., Jamali, A.M., Ullmann, C.V., Voigt, S., Cocquerez, T., 2018. Integrated stratigraphy of the Late Cretaceous Gurpi Formation (Iran): a new reference for the eastern Tethys and implications for large-scale correlation of stage boundaries. *Cret. Res. 91*, 312–340.

Razmjooei, M.J., Thibault, N., Kani, A., Ullmann, C.V. and Jamali, A.M., 2020a. Santonian-Maastrichtian carbon-isotope stratigraphy and calcareous nannofossil biostratigraphy of the Zagros Basin: Long-range correlation, similarities and differences of carbon-isotope trends at global scale. *Global Planet. Change 184*, 103075.

Razmjooei, M.J., Thibault, N., Kani, A., Dinarès-Turell, J., Pucéat, E., Chin, S., 2020b. Calcareous nannofossil response to Late Cretaceous climate change in the eastern Tethys (Zagros Basin, Iran). *Palaeogeogr. Palaeoclimatol. Palaeoecol. 538*, 109418.

Reischmann, T., Kröner, A., 1994. Late Proterozoic island arc volcanics from Gebeit, Red Sea Hills, northeast Sudan. *Geologische Rundschau 83*, 547–563.

Revel, M., Ducassou, E., Grousset, F.E., Bernasconi, S.M., Migeon, S., Revillon, S., Mascle, J., Murat, A., Zaragosi, S., Bosch, D., 2010. 100,000 Years of African monsoon variability

recorded in sediments of the Nile margin. *Quart. Sci. Rev. 29*, 1342–1362.

Robinson, S.A., Murphy, D.P., Vance, D., Thomas, D.J., 2010. Formation of "Southern Component Water" in the Late Cretaceous: Evidence from Nd-isotopes. *Geology 38*, 871–874.

Robinson, S.A., Vance, D., 2012. Widespread and synchronous change in deep-ocean circulation in the North and South Atlantic during the Late Cretaceous: Currents. *Paleoceanography 27*, 1–8.

Rostami, M.A., Leckie, R.M., Font, E., Frontalini, F., Finkelstein, D., Koeberl, C., 2018. The Cretaceous-Paleogene transition at Galanderud (nothern Alborz, Iran): a multidisciplinay approach. *Palaeogeogr. Palaeoclimatol. Palaeoecol. 495*, 82–101.

Royer, D.L., Pagani, M., Beerling, D.J., 2012. Geobiological constraints on Earth system sensitivity to CO_2 during the Cretaceous and Cenozoic. *Geobiology 10*, 298–310.

Salaj, J., Nairn, A.E.M., 1987. Age and depositional environment of the Lower Tár "Member" of the Zimám Formation (Upper Senonian) in the Northern Hamada Al Hamra, Libya. *Palaeogeogr. Palaeoclimatol. Palaeoecol. 61*, 121–143.

Saura, E., Verges, J., Homke, S., Blanc, E., Serra-Kiel, J., Bernaola, G., Casciello, E., Fernandez, N., Romaire, I., Casini, G., Embry, J.C., Sharp, I.R., Hunt, D.W., 2011. Basin architecture and growth folding of the NW Zagros early foreland basin during the Late Cretaceous and early Tertiary. *J. Geol. Soc. London, 168*, 235–250.

Saccani, E., Allahyari, K., Beccaluva, L., Bianchini, G., 2013. Geochemistry and petrology of the Kermanshah ophiolites (Iran): implication for the interaction between passive rifting, oceanic accretion, and OIB-type components in the southern Neo-Tethys Ocean. *Gondw. Res. 24*, 392–411.

Schopka, H.H., Derry, L.A., Arcilla, C.A., 2011. Chemical weathering, river geochemistry and atmospheric carbon fluxes from volcanic and ultramafic regions on Luzon Island, the

Philippines. *Geochim. Cosmochim. Acta 75*, 978–1002.

Şengör, A.C., Stock, J., 2014. The Ayyubid Orogen: an ophiolite obduction-driven orogen in the late Cretaceous of the Neo-Tethyan south margin. *Geosci. Canada 41*, 225–254.

Shafaii Moghadam, H., Stern, R.J., 2011. Geodynamical evolution of Upper Cretaceous Zagros ophiolites: formations of oceanic lithosphere above a nascent subduction zone. *Geol. Mag. 148*, 762–801.

Shafaii Moghadam, H., Stern, R., 2014. Ophiolites of Iran: Keys to understanding the tectonic evolution of SW Asia: (I) Paleozoic ophiolites. *J. of Asian Earth Sciences* 91, 19–38.

Shafaii Moghadam, H., Stern, R.J., 2015. Ophiolites of Iran: Keys to understanding the tectonic evolution of SW Asia: (II) Mesozoic ophiolites. *J. Asian Earth Sci.* 100, 31–59.

Shafaii Moghadam, H., Mosaddegh, H., Santosh, M., 2012. Geochemistry and petrogenesis of the Late Cretaceous Haji-Abad ophiolite (Outer Zagros Ophiolite Belt, Iran): implications for geodynamics of the Bitlis-Zagros suture zone. *Geol. J. 48.*

Shafaii Moghadam, H., Stern, R.J., Chiaradia, M., Rahgoshay, M., 2013. Geochemistry and tectonic evolution of the Late Cretaceous Gogher-Baft ophiolite, central Iran. *Lithos 16-169*, 33–47.

Shahidi, M., Nazari, N., 1997. Geological map of Harsin, 1/100.000 scale. Tehran: Geological survey of Iran.

Soudry, D., Segal, I., Nathan, Y., Glenn, C.R., Halicz, L., Lewy, Z., VonderHaar, D.L., 2004. ^{44}Ca/^{42}Ca and ^{143}Nd/^{144}Nd isotope variations in Cretaceous-Eocene Tethyan francolites and their bearing on phosphogenesis in the southern Tethys. *Geol. Soc. Amer. 32*, 389–392.

Soudry, D., Glenn, C.R., Nathan, Y., Segal, I., Von der Haar, D., 2006. Evolution of Tethyan phosphogenesis along the northern edges of the Arabian–African shield during the Cretaceous–Eocene as deduced from temporal variations of Ca and Nd isotopes and rates

of P accumulation. *Earth Sci. Rev. 78*, 27–57.

Stacey, J.S., Hedge, C.E., 1984. Geochronologic and isotopic evidence for early Proterozoic crust in the eastern Arabian Shield. *Geology 12*, 310–313.

Stein, M., Goldstein, S.L., 1996. From plume head to continental lithosphere in the Arabian–Nubian shield. *Nature 382*, 773–778.

Stern, R.J., 1994. Arc assembly and continental collision in the Neoproterozoic East African Orogen: Implications for the assembly of Gondwana land. *Annual Rev. Earth Planet. Sci. 22*, 319–351.

Stern, R.J., 2002. Crustal evolution in the East African Orogen: a neodymium isotopic perspective. *J. Afri. Earth Sci. 34*, 109–117.

Stern, R.J., Abdelsalam, M.G., 1998. Formation of juvenile continental crust in the Arabian-Nubian shield: evidence from granitic rocks of the Nakasib suture, NE Sudan. *Geologische Rundschau 87*, 150–160.

Stoeser, D.B., Frost, C.D., 2006. Nd, Pb, Sr, and O isotopic characterization of Saudi Arabian shield terranes. *Chem. Geol. 226*, 163–188.

Tanaka, T., Togashi, S., Kamioka, H., Amakawa, H., Kagami, H., Hamamoto, T., Yuhara, M., Orihashi, Y., Yoneda, S., Shimizu, H., et al., 2000. JNdi-1: a neodymium isotopic reference in consistency with LaJolla neodymium. *Chem. Geol. 168*, 279–281.

Tantawy, A.A., Keller, G., Adatte, T., Stinnesbeck, W., Kassab, A., Schulte, P., 2001. Maastrichtian to Paleocene depositional environnement of the Dakhla Formation, Western Desert, Egypt: sedimentology, mineralogy and integrated micro- and macrofossil biostratigraphies. *Cret. Res. 22*, 795–827.

Taylor, S.R., McLennan, S.M., 1985. The continental crust: its composition and evolution. Blackwell, Oxford, pp. 312.

Tessier, A., Campbell, P.G.C., Bisson, M., 1979. Sequential extraction procedure for the speciation of particulate trace metals. *Analytical Chem. 51*, 844–851.

Tilton, G.R., Hopson, C.A., Wright, J.E., 1981. Uranium-lead isotopic ages of the Samail Ophiolite, Oman, with applications to Tethyan ocean ridge tectonics. *J. Geophy. Res. Solid Earth 86*, 2763–2775.

Thiry, M., Jacquin, T., 1993. Clay mineral distribution related to rift activity, sea-level changes and paleoceanography in the Cretaceous of the Atlantic Ocean. *Clay Min. 28*, 61–84.

Thomas, D.J., 2004. Evidence for deep-water production in the North Pacific Ocean during the early Cenozoic warm interval. *Nature 430*, 65–68.

Thomas, D.J., Korty, R., Huber, M., Schubert, J.A., Haines, B., 2014. Nd isotopic structure of the Pacific Ocean 70–30 Ma and numerical evidence for vigorous ocean circulation and ocean heat transport in a greenhouse world. *Paleoceanography 29*, 454–469.ope paleothermometry. *Geology 42*, 351–354.

Tostevin, R., Shields, G.A., Tarbuck, G.M., He, T., Clarkson, M.O., Wood, R.A., 2016. *Chem. Geol. 438*, 146–162.

Upchurch, G. R., Kiehl, J., Schields, C., Scherer, J., Scotese, C., 2015. Latitudinal temperature gradients and high-latitude temperatures during the latest Cretaceous: congruence of geological data and climate models. *Geology 43*, 683–689.

Vanderaveroet, P., Averbuch, O., Deconinck, J.-F., Chamley, H., 1999. A record of glacial/interglacial alternations in Pleistocene sediments off New Jersey expressed by clay mineral, grain-size and magnetic susceptibility data. *Marine Geology 159*, 79–92.

Van der Meer, D.G., Zeebe, R., Van Hisbergen, D.J.J., Sluijs, A., Sparkman, W., Torsvik, T.H., 2014. Plate tectonic controls on atmospheric CO_2 levels since the Triassic. *Proc. Natl. Acad. Sci. U.S.A.* 111, 4380–4385.

Van der Lubbe, H.J.L., Franck, M., Tjallingii, R., Schneider, R.R., 2016. Neodymium isotope constraints on provenance, dispersal, and climate-driven supply of Zambezi sediments along the Mozambique Margin during the past ~45,000 years. *Geochem. Geophy. Geosys. 17*, 181–198.

Voigt, S., Jung, C., Friedrich, O., Frank, M., Teschner, C., Hoffmann, J., 2013. Tectonically restricted deep-ocean circulation at the end of the Cretaceous greenhouse. *Earth Planet. Sci. Lett. 369–370*, 169–177.

Wang, Y., Huang, C., Sun, B., Quan, C., Wu, J., Lin, Z., 2014. Paleo-CO_2 variation trends and the Cretaceous greenhouse climate. *Earth Sci. Rev. 129*, 136–147.

Webb, G.E., Kamber, B.S., 2000. Rare earth elements in Holocene reefal microbialites: a new shallow seawater proxy. *Geochim. Cosmochim. Acta 9*, 1557–1565.

Whitechurch, H., Omrani, J., Agard, P., Humbert, F., Montingny, R., Jolivet, L., 2013. Evidence for Paleocene-Eocene evolution of the foot of the Eurasian margin (Kermashah ophiolite, SW Iran) from back-arc to arc: implications for regional geodynamics and obduction. *Lithos 182 – 183*, 11–32.

Whitehouse, M.J., Windley, B.F., Ba-Batt, M.A.O., Faning, C.M., Rex, D.C., 1998. Crustal evolution and terrane correlation in the eastern Arabian Shield, Yemen: geochronological constraints. *J. Geol. Soc. 155*, 281–296.

Whitehouse, M.J., Windley, B.F., Stoeser, D.B., Al-Khirbash, S., Ba-Bttat, M.A., Haider, A., 2001. Precambrian basement character of Yemen and correlations with Saudi Arabia and Somalia. *Precamb. Res. 105*, 357–369.

Weis, D., Kieffer, B., Maerschalk, C., Barling, J., de Jong, J., Williams, G.A., Hanano, D., Pretorius, W., Mattielli, N., Scoates, J.S., 2006. High-precision isotopic characterization of USGS reference materials by TIMS and MC-ICP-MS. *Geochem. Geophy. Geosys. 7*, 1–30.

Wilson, D.J., Piotrowski, A.M., Galy, A., Clegg, J.A., 2013. Reactivity of neodymium

carriers in deep sea sediments: Implications for boundary exchange and paleoceanography. *Geochim. Cosmochim. Acta 109*, 197–221.

Winterer, E.L., 1991. The Tethyan Pacific during Late Jurassic and Cretaceous times. *Palaeogeogr. Palaeoclimatol. Palaeoecol 87*, 253–265.

Zarei, E., Ghasemi-Nejad, E., 2015. Sequence stratigraphy of the Gurpi Formation (Campanian–Paleocene) in southwest of Zagros, Iran, based on palynomorphs and foraminifera. *Arab. J. Geosci. 8*, 4011–4023.

Figures and Tables

Figure 1: Structural map of the western Iranian domain (modified from Homke et al., 2009) replaced on a google earth picture (A), palaeogeographical maps of the eastern Tethyan Realm during the early Campanian (B) and late Maastrichtian (C; modified from Barrier and Vrielynck, 2007). Abbreviations: TCC = Tethyan Circum global Current; *Zag. Bas.* = Zagros Basin.

Figure 2: Field view of the Shahneshin section (Zagros Basin, Iran) (A) uppermost Santonian to lowemost Campanian stratigaphic succession and (B) upper Campanian stratigraphic succession.

Figure 3: Clay mineralogy of the Shahneshin section compared with the $\varepsilon_{Nd(t)}$ of the acetic acid leachates and of the insoluble fractions, and with the Ni/Al [(Ni(ppm)/Al(%))x10 000] and Cr/Al [(Cr(ppm)/Al(%)x10 000] ratios. These data have been replaced along the lithological succession, the calcareous nannofossils and planktonic foraminifera biostratigraphy and the δ^{13}C bulk rock curve of Razmjooei et al. (2018). The 2σ error are 0.35 ε-units for the insoluble fraction and 0.21 ε-units for the acetic acid leachate fraction.

Abbreviations: C = Coniacian ; Maast. = Maastrichtian ; Sa = Santonian

Figure 4: X-ray diffractograms of the clay fraction of some samples from the Shahneshin section, at 81m, 234m and 313m. The comparison of the X-ray diffractograms below 250 m

(at 81m and 234m) and above 250 m (at 313m) highly suggests the presence of vermiculite with high and narrow 14Å peak in the upper part of the section. This difference reflects the probable occurrence of vermiculite.

Figure 5: PAAS-normalized REE patterns for acetic acid leachates (at the top) and insoluble fractions (at the bottom) of the Shahneshin samples.

Figure 6: Evolution of the proportions of illite, chlorite and kaolinite compared with $\varepsilon_{Nd(t)}$ of the local bottom seawater and of the insoluble fraction at Shahneshin, and the Ni/Al and Cr/Al ratios, during the Late Cretaceous. The relative ages have been calculated using the new age-model established for the Shahneshin section (see Table 1 and Suppl. Fig. 1., modified from Razmjooei et al., 2018, based on GTS 2016 from Ogg et al., 2016). The 2σ error are 0.35 ε-units for the insoluble fraction and 0.21 ε-units for the local bottom seawater. $\Delta\varepsilon_{Nd(t)}$ represent the difference between $\varepsilon_{Nd(t)}$ of the seawater and the insoluble fraction. TEX86 palaeotemperature data are from Pama quarry (Israel), Adrehet 1 borehole (Israel; Alsenz et al., 2013) and Shulqualak-Evans borehole (Linnert et al., 2014) and $\delta^{18}O_{planktonic\ foraminifera}$ palaeotemperature data from ODP Site 1259 (Bornemann et al., 2008), ODP Site 1050 (Huber et al., 2002; O'Brien et al., 2017) and ODP Site 762 (Falzoni et al., 2016). These palaeo sea surface temperature are replaced along age model from O'Brien et al. (2017), based on GTS 2012 (Gradstein et al., 2012)

Figure 7: Nd isotopic composition (ε_{Nd}) calculated at 80Ma (references and calculation in Suppl. Table 1) of different magmatic complexes outcropping in the general area of the Zagros Basin. Present-day extension of the Arabian-Nubian Shield (dark grey), terrane delimitation, and Precambrian deposition basins (dashed outline) from Johnson and Woldehaimanot (2003).

Abbreviations: EG = Eastern Gulf Basin; F = Fahud Basin; G = Ghudun Basin; Gh = Ghaba Basin; SO = South Oman Basin; WG = Western Gulf Basin. The hatched area corresponds to

the western oceanic arc, and the dotted area to the eastern oceanic arc, as defined in Stoeser and Frost (2006).

Table 1: Eight anchor points used to build the age-model for the Shahneshin section (updated from Razmjooei et al., 2018 taking into account the new results on Bowan section presented in Razmjooei et al., 2020a).

Table 2: REE concentrations and Nd isotopic data of the insoluble fraction, the acetic acid leachate of the Shahneshin section and the certified reference material used in the analytic series. $\varepsilon_{Nd(t)}$ values of the Shahneshin section's samples have been calculated using the age-model of Table 1.

Table 2: Bulk rock major and trace element concentrations of the samples from the Shahneshin section.

Supplementary materials

Supplementary Figure 1: Age-depth model for the Shahneshin section derived from linear interpolations across the depth and ages of eight anchor points of Table 1. The Coniacian/Santonian boundary is readjusted at 40 m, corresponding to the level of the identified Kingsdown Event. GTS2016: Ogg et al. (2016)

Supplementary Table 1: Compilation of the ε_{Nd} data from Zagros region and up to the Arab-Nubian shield

Supplementary Table 2: Compilation of the measured data presented in this study

Stratigraphic anchors	Height (m)	Age (Ma)	Sedimentation rate (cm/kyr)
K-Pg Boundary	345,85	66,04	-
Base Maastrichtian	283,8	72,15	1,02
Base hiatus in Razmjooei agemodel	283,8	74,01	0,00
FO *G. aegytiaca*	274	74,42	2,39
LO *M. furcatus*	113	81,00	2,45
LO *D. asymetrica*/Base Campanian	94	84,20	0,59
Kingsdown event/Base Santonian	40	86,49	2,36

Base section with constant sedimentation rate	0	88,19	2,36

FO = First Occurrence; LO = Last Occurrence

Sample ID	Depth (m)	Age (Ma)	La (ppm)	Ce (ppm)	Pr (ppm)	Nd (ppm)	Sm (ppm)	Eu (ppm)	Gd (ppm)	Tb (ppm)	Dy (ppm)	Ho (ppm)	Er (ppm)	Tm* (ppm)	Yb (ppm)	Lu (ppm)	^{147}Sm/^{144}Nd	^{143}Nd/^{144}Nd	2s	εNd(t)	2s

Insoluble fractions (n=17)

Sample ID	Depth (m)	Age (Ma)	La	Ce	Pr	Nd	Sm	Eu	Gd	Tb	Dy	Ho	Er	Tm*	Yb	Lu (ppm)	^{147}Sm/^{144}Nd	^{143}Nd/^{144}Nd	2s	εNd(t)	2s
ShGE18	3.0	67.31	17.55	27.1	2.85	9.77	1.63	0.33	1.52	0.29	2.3	0.86	2.12	0.33	2.51	0.38	0.103	0.512128	0.000006	-9.01	0.15
ShGE17	31.0	69.47	11.18	19.17	2.02	7.42	1.24	0.28	1.27	0.29	1.45	0.32	1.28	0.23	1.48	0.28	0.110	0.512200	0.000008	-7.63	0.19
ShGE16	29.25	71.29	14.41	20.16	2.19	6.81	1.32	0.30	1.08	0.44	1.69	0.34	1.23	0.22	1.61	0.25	0.097	0.512145	0.000005	-8.56	0.13
ShGE15	27.10	74.54	12.7	17.1	1.86	6.21	1.10	0.28	1.05	0.59	1.94	0.32	1.27	0.23	1.77	0.26	0.108	0.512217	0.000011	-7.22	0.25

																		1		
ShGE13	232.0	76.14	16.6	23.8	2.46	8.13	1.46	0.292	1.17	0.223	1.66	0.411	1.47	0.23	1.77	0.27	0.109	0.512254	0.000009	-6.49	0.21
ShGE12	211.7	76.97	16.4	21.3	2.11	6.71	1.05	0.198	0.89	0.161	1.23	0.318	1.15	0.18	1.39	0.22	0.094	0.512222	0.000005	-6.95	0.14
ShGE11	192.0	77.77	17.6	25	2.53	8.29	1.53	0.276	1.25	0.239	1.74	0.42[illegible]	[illegible].5	0.24	1.85	0.29	0.112	0.512268	0.000008	-6.23	0.20
ShGE10	171.1	78.63	17	24.8	2.57	8.6	1.54	0.318	1.34	0.241	1.76	0.418	1.46	0.23	1.68	0.26	0.108	0.512250	0.000011	-6.53	0.25
ShGE09	152.0	79.41	15.2	21.5	2.26	7.69	1.3	0.234	1.04	0.186	1.45	0.368	1.25	0.19	1.46	0.24	0.103	0.512192	0.000013	-7.60	0.29
ShGE08	132.9	80.19	20.6	27	2.79	9.19	1.46	0.287	1.18	0.210	1.61	0.406	1.42	0.23	1.72	0.27	0.096	0.512174	0.000006	-7.87	0.17
ShG	113	81.00	19.	26.	3.0	10.	1.9	0.	1.9	0.	2.3	0.	1.8	0.	1.9	0.31	0.112	0.51	0.0	-6.	0.2

Sample		Mean	…		
E07	. 0 0		5 2 2 7 9 4 7 3 3 5 4 2 9		
ShGE06	9.8	84.29	…	0.19	0.108
ShGE05	7.4	85.04	…	0.22	0.100
ShGE04	6.0	85.64	…	0.17	0.102
ShGE03	3.9	86.50	…	0.32	0.111
ShGE02	2.2	87.26	…	0.21	0.095
ShGE01	1.0	88.15	…	0.24	0.102

		4	
2s external reproducibility:	**± 0.004**	**± 0.0016**	**± 0.035**

Acetic acid leachate (n=18)

Sample										
ShGE18	3.30	67.31	0.059	0.117	0.5123	0.0016	-4.57	0.17
ShGE17	3.10	69.47	0.064	0.122	0.5165	0.0016	-4.52	0.14
ShGE16	2.95	71.29	0.048	0.122	0.5140	0.0016	-3.86	0.19
ShGE15	2.70	74.54	0.070	0.122	0.5120	0.0017	-3.79	0.17
ShGE12	2.52	75.31	0.082	0.124	0.5123	0.0010	-4.01	0.14

4

8 0
5 0
5
0

S
h 2
G 3
E 2
1 .
3 0 76.14

S
h 2
G 1
E 1
1 .
2 7 76.97

S
h 1
G 9
E 2
1 .
1 0 77.77

S
h 1
G 7
E 1
1 .
0 1 78.63

S
h 1
G 5
E 2
0 .
9 0 79.41

S
h 1
G 3
E 2
0 .
8 9 80.19
S 1 81.00

hGE07	1 3 . 0		8	8	1 9 .	7 5 .	9 1 .	2 2 0 7	1 5 8	1 2 1	0 3	2 9	6 9	0 2 4	8	5 1 2 3 3 9	. 0 0 0 0 0 5 0
ShGE06	9 1 . 8	84.29	7 . .	5 . .	0 9 2	4 6 7	0 9 6	0. 1 2 2 1	1 . 4 7 1	1 . 2 1 4	0. 1 6 9	0 6 8 4	0. 0 8 8	0.11 7	0.125	4 . 1 2 3 2	0 0 5 . 1 2 . 1 9

1

										6	0
										5	0
											6

| | 2s external reproducibility: | ± 0.004 | ± 0.000009 | ± 0.021 |

REE concentrations in Certified reference material

USGS BHVO-2 — Average (n=10):

```
            2   2       0       0       0 2
Avera   1 3 5 3 5 . 6 . 5 . 2 . .
ge      4 6 . . . 0 . 9 . 9 . 3 0
(n=10)  8 2 5 9 8 0 7 5 3 0 3 0 9 8      0.27 8        0.1508
```

reference values (Jochum et al., 2016):

```
        3 5 2 6 2 6 0 ? 0 1
        1 7 . 4 . . . ? . 2 . .
        5 . 3 . 0 0 2 9 . 3 9
        . 5 3 2 2 4 0 3 ? 8 5 3 9
        2 3 9 7 3 3 7 ? 3 9 1 5 4      0.27 5        0.1501
```

RSD (%):

```
        -2 -3 -3 -2 -2 -? -2 -3 -0 -1 -0 -3 -0
         .7 .6 .6 .8 .4 .? .1 .6 .9 .9 .6 .3 .8   0.8      0.5
```

USGS BCR-2 — Average (n=7):

```
                    1       1           0
Avera   2 5 6 2 6 . 6 . 6 1 3 . 3
ge      5 3 . 8 . 9 . 0 . . . 5 .
(n=7)   4 4 1 5 4 5 1 9 8 2 4 0 0      0.52 0        0.139
```

reference values (Jochum et al., 2016):

```
        2 5 6 2 6 1 6 1 6 1   0 3
        5 3 . 8 . . . . . .   3 . .
        . . 8 . 5 9 8 0 4 3   5 3
        0 2 7 6 7 9 1 7 2 1 3 9      0.50 5        0.138
```

:

RSD (%)	1.4	0.6	0.2	0.9	0.1	-2.2	0.0	-2.6	0.9	0.5	1.9	-3.2	-3.2	3.0	-1.0

Reproducibility of the Isotopic measurements of the UGSS BHVO-2 certified reference material

Reference value (MC-ICP-MS, Weis al., 2006):	0.512990	0.000010
average value during the insoluble fraction measurements (JNdi-1 bracketing, n=5):	0.512987	0.0000005
average value during the acetic leachate measurements (Rennes-in-house Nd standard bracketing, n=12):	0.512988	0.0000007

Sample ID	SiO$_2$ (%)	Al$_2$O$_3$ (%)	Fe$_2$O$_3$ (%)	MnO (%)	MgO (%)	CaO (%)	Na$_2$O (%)	K$_2$O (%)	TiO$_2$ (%)	P$_2$O$_5$ (%)	Ni (ppm)	Cr (ppm)
G3	9.43	4.72	1.56	< D.L.	0.39	44.57	0.04	0.60	0.18	< D.L.	33.2	63.4
G10	15.39	6.95	2.44	< D.L.	0.51	38.77	0.05	1.02	0.31	< D.L.	33.6	76.6
G22	10.80	3.63	1.42	< D.L.	0.44	44.62	0.05	0.82	0.17	0.12	31.3	45.6
G23	12.21	4.39	1.65	< D.L.	0.46	43.14	0.03	0.94	0.20	0.12	29.9	45.9
G25	13.84	5.15	2.10	0.037	0.49	41.22	0.04	1.09	0.23	0.11	65.6	47.5

G26	13.65	5.06	1.68	< D.L.	0.47	41.73	0.04	1.08	0.23	0.13	22.9	42.4
G32	18.36	6.65	2.26	0.016	0.58	36.61	0.07	1.58	0.31	0.11	46.9	53.4
G38	15.00	4.92	1.76	< D.L.	0.57	40.84	0.06	1.44	0.23	0.12	22.6	40.3
G48	15.25	3.86	1.52	< D.L.	0.57	41.53	0.08	1.14	0.17	0.10	29.2	42.4
G51	12.57	3.18	1.31	< D.L.	0.45	44.02	0.06	0.90	0.14	< D.L.	22.6	33.6
G55	16.27	4.91	1.86	< D.L.	0.64	39.89	0.04	1.17	0.23	< D.L.	32.3	49.7
G60	12.45	4.03	1.52	< D.L.	0.53	43.48	0.03	0.87	0.19	< D.L.	21.1	48.0
G73	10.08	3.32	1.38	< D.L.	0.41	45.88	0.03	0.51	0.15	< D.L.	26.4	47.6
G74	11.23	4.17	1.59	< D.L.	0.44	44.31	0.07	0.55	0.19	< D.L.	32.5	56.9
G82	11.88	4.32	1.70	< D.L.	0.43	43.65	0.05	0.55	0.20	0.10	29.8	58.4
G83	10.99	3.81	1.68	< D.L.	0.45	44.52	0.05	0.51	0.18	0.11	29.0	61.5
G88	11.70	4.52	1.62	< D.L.	0.44	43.31	0.03	0.54	0.21	< D.L.	37.3	66.1
G94	11.44	3.87	1.66	< D.L.	0.54	44.03	0.10	0.61	0.18	0.19	40.8	101
G96	11.30	3.47	1.59	< D.L.	0.54	44.30	0.07	0.60	0.17	< D.L.	48.5	89.8
G102	8.73	2.14	1.14	0.018	0.51	47.89	0.11	0.43	0.11	< D.L.	41.3	53.3
G108	7.63	1.99	1.00	< D.L.	0.52	48.27	0.07	0.40	0.10	< D.L.	40.0	65.7
G120	12.41	3.24	2.09	0.025	1.06	43.59	0.10	0.69	0.18	0.11	83.4	98.5

Declaration of interests

☒ The authors declare that they have no known competing financial interests or personal relationships that could have appeared to influence the work reported in this paper.

☐The authors declare the following financial interests/personal relationships which may be considered as potential competing interests:

Highlights

- Alternating humid and arid periods throughout the Late Cretaceous of Zagros
- Ophiolite sequence was aerially exposed as soon as the Coniacian in the Zagros area
- Intensification of the TCC from the middle Campanian to the Maastrichtian
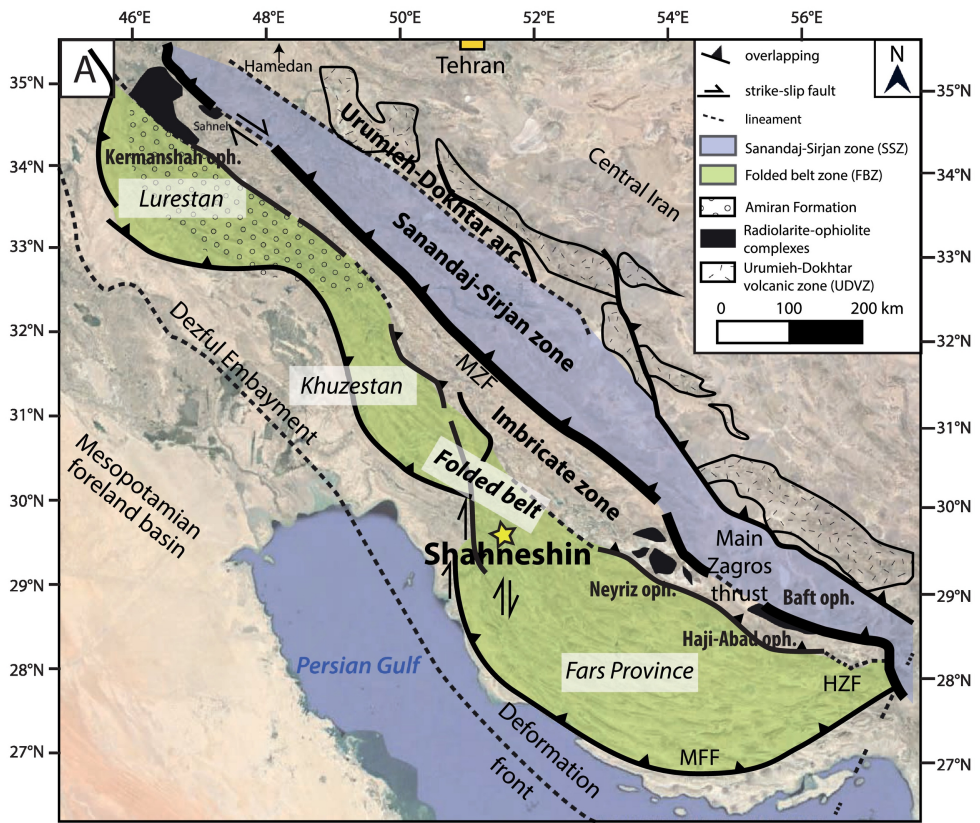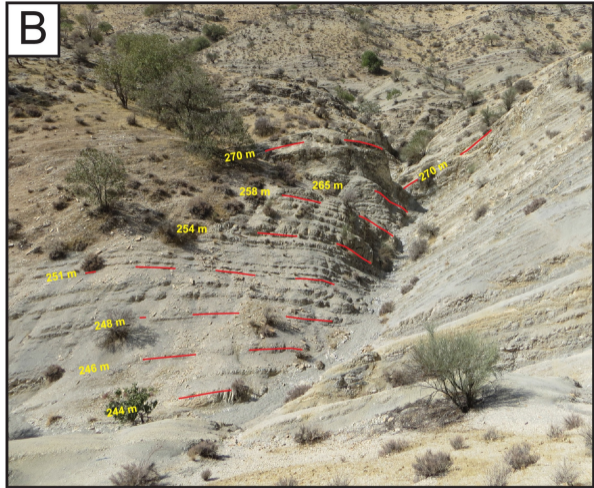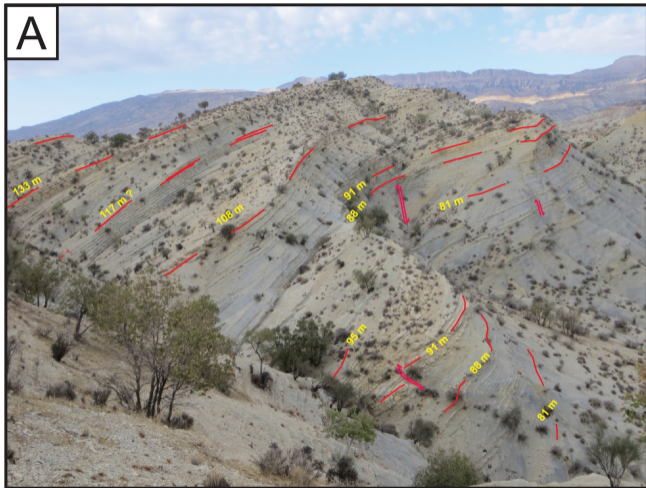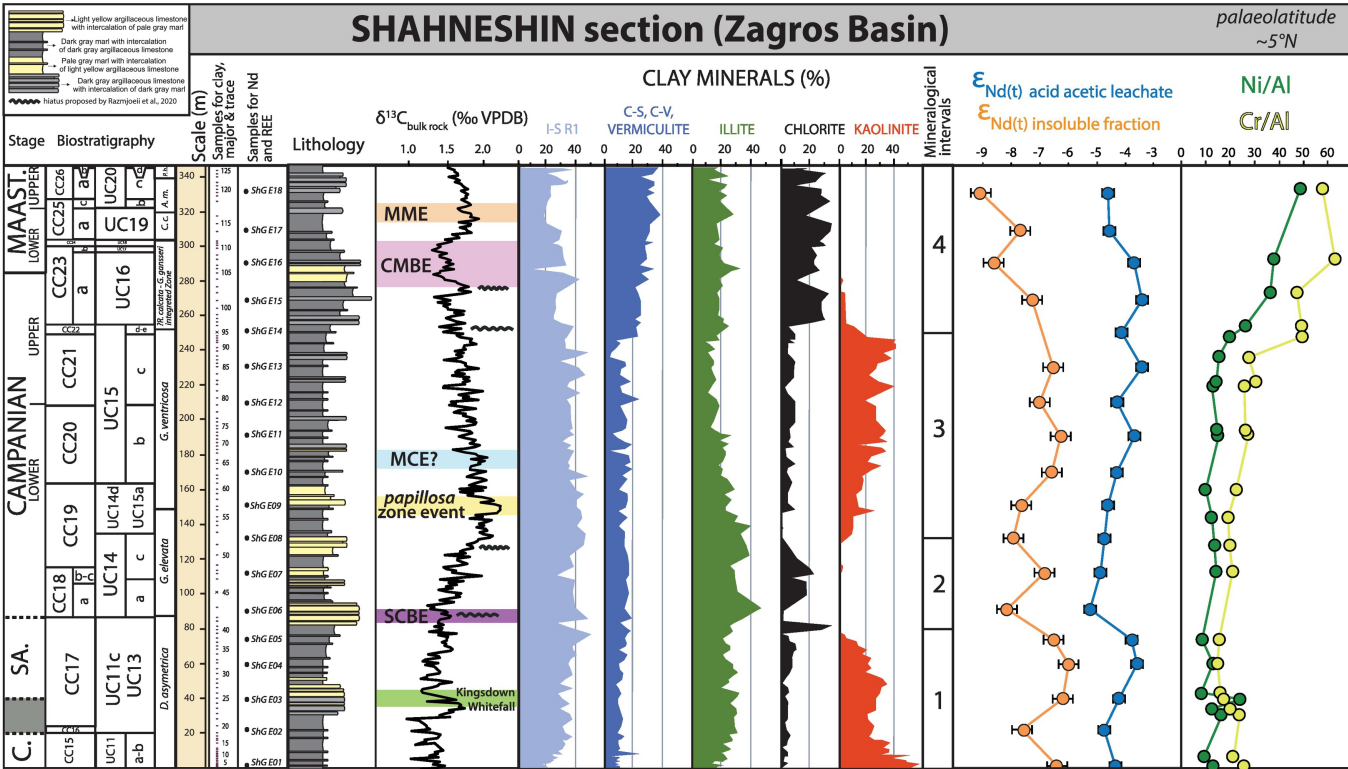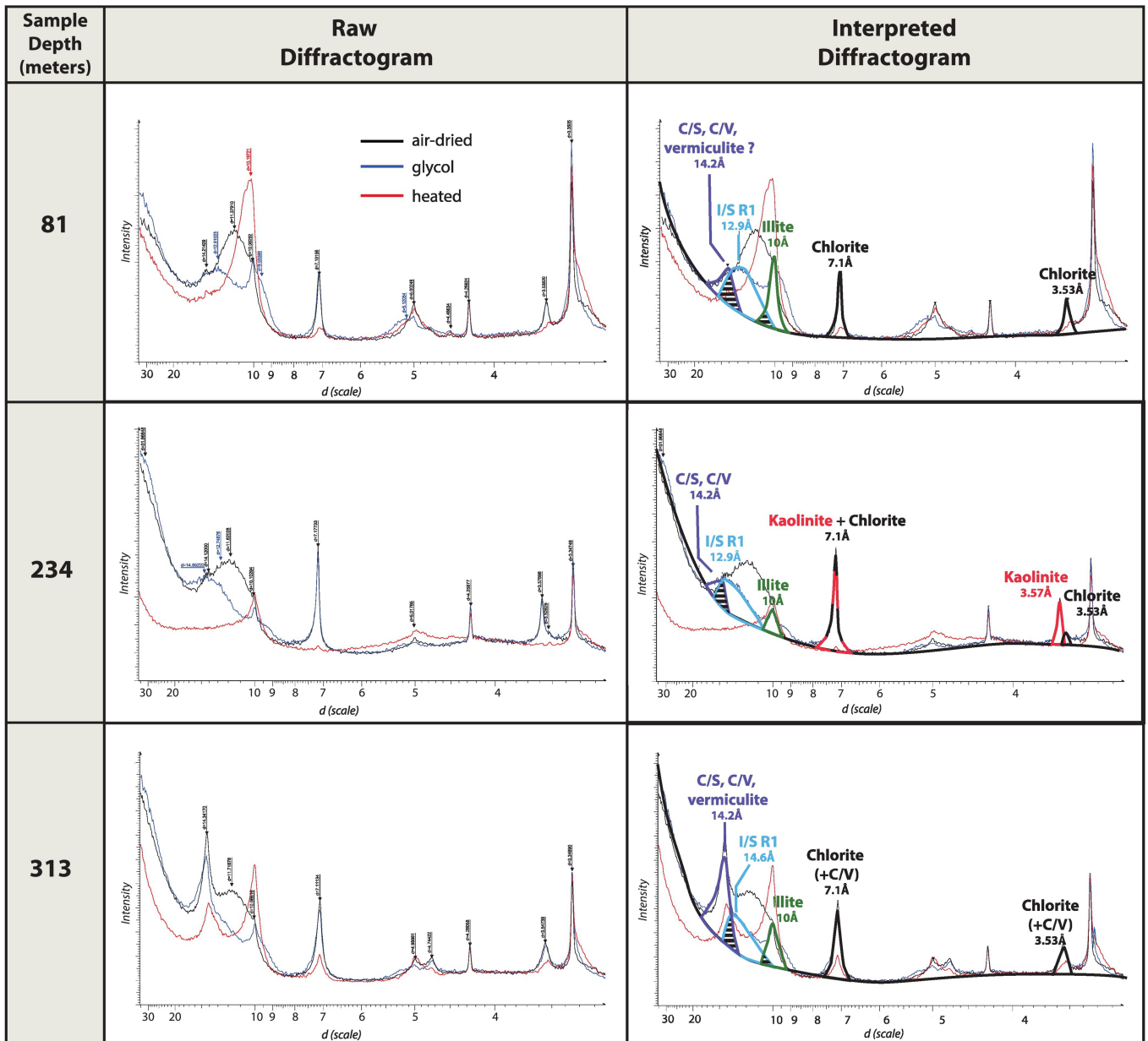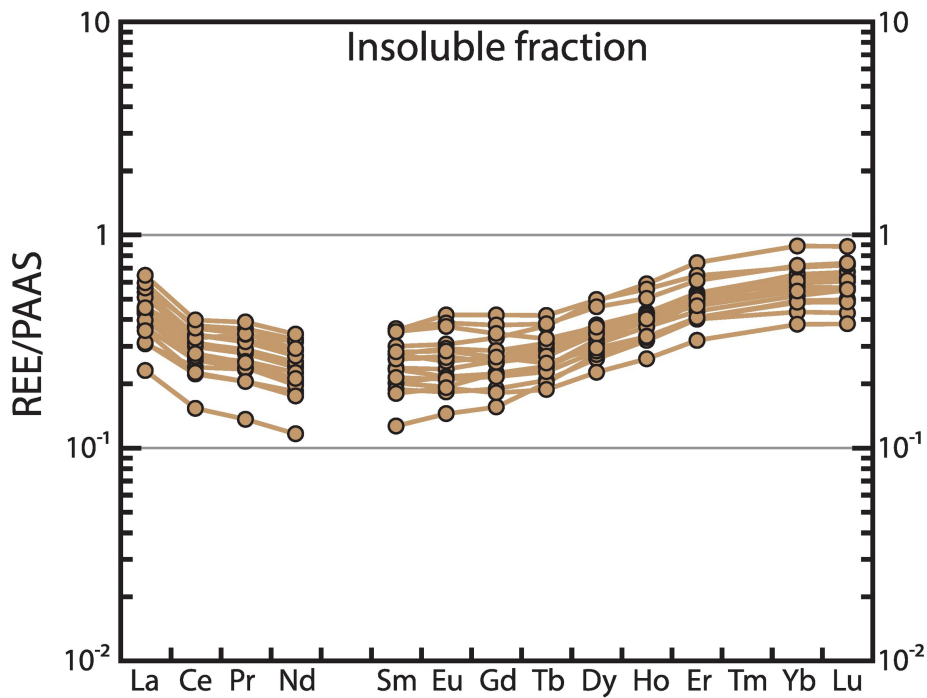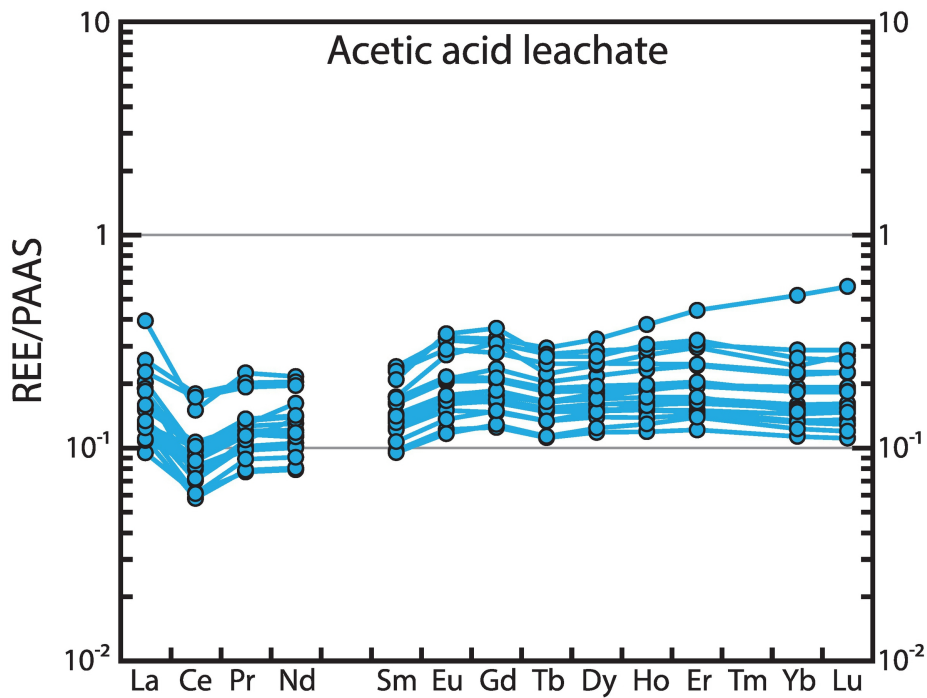
Figure 1

Figure 2
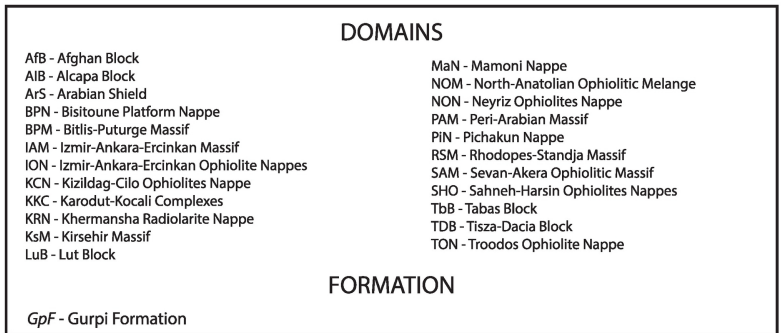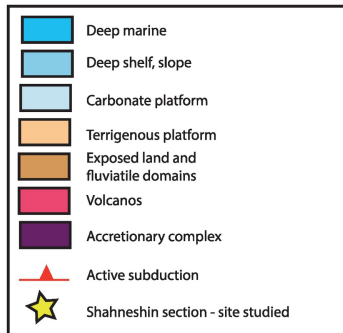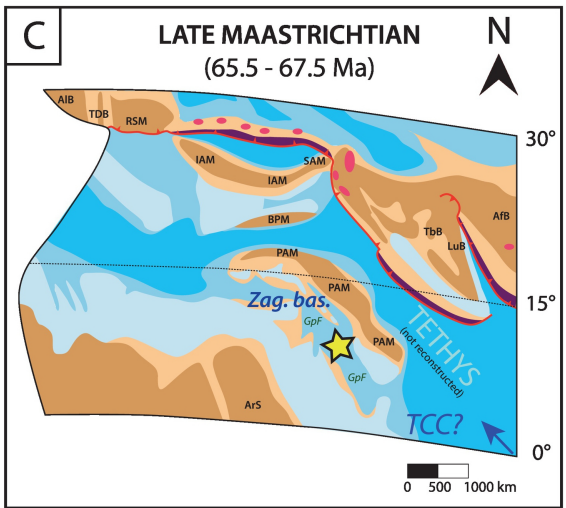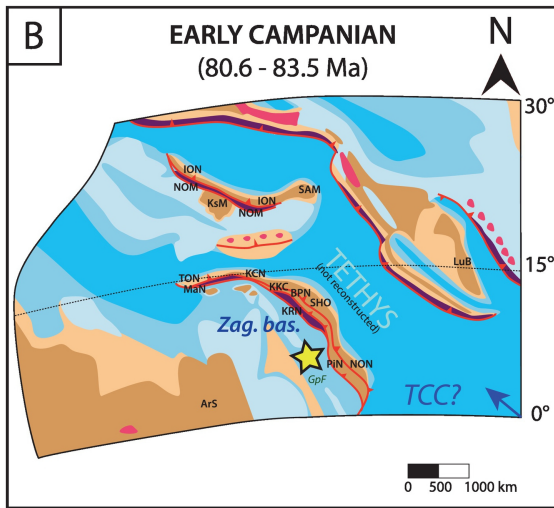
Figure 3

Figure 4

Figure 5

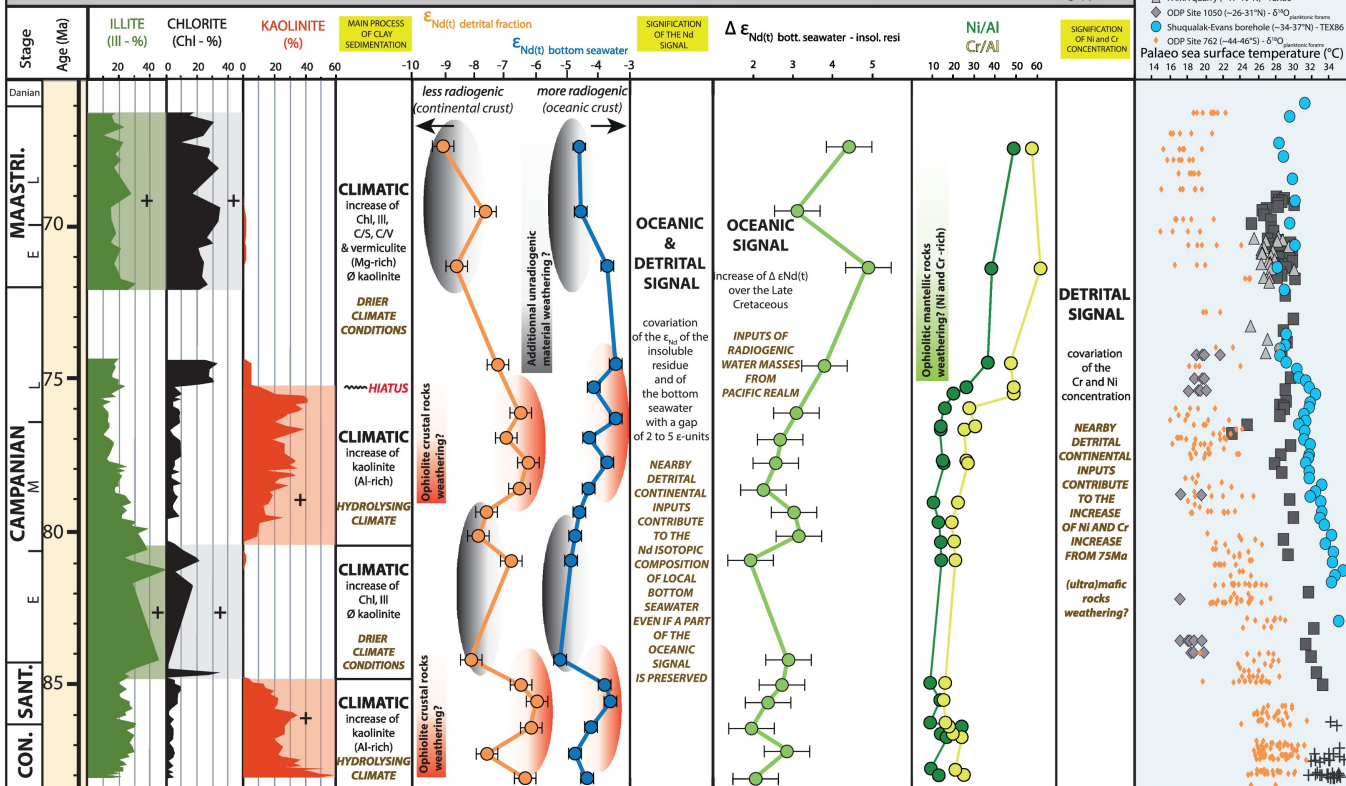Figure 6

PRESENT DAY - Nd isotopic composition (ε_{Nd})

Misho plutonic complex:
-4 to 1.2 ε-units
(although two samples yield -6.4 and
-9.7 ε-units)

Tuyeh-Darvar granitoid:
-3.5 to -2.9 ε-units

Harsin-Sahneh serpentinized
peridotites: **-7.8 to 7.4 ε-units**

Matwat mafic complex:
4.9 to 7.9 ε-units

Deshir ophiolite:
6.6 to 8.6 ε-units

Neyriz ophiolite:
7.8 to 9.8 ε-units

western arc:
-4.3 to 18.3 ε-units

eastern arc:
-4.2 to 6.5 ε-units

Makran ophiolite:
5.1 to 9.3 ε-units

metarhyolite:
2.5 ε-units

gneiss:
-35.2 to -8.5 ε-units

alcali granite:
1.0 ε-units

oceanic arc:
-3.8 to 6.7 ε-units

Khida terrane:
-23.8 to -6.3 ε-units

ophiolite:
-5.2 to 17.8 ε-units

metasediment:
-17.3 to -8 ε-units

granitoid & gneisses:
-27.7 to 0.1 ε-units

oceanic arc:
-0.8 to 2.9 ε-units

oceanic arc:
-4.5 to 9.3 ε-units

metasediments:
-20.7 to -11.1 ε-units

Shahneshin

Figure 7